





Article

Comparison of Drivetrain Topologies for an Ankle Gait Cycle

Yentl Joos ^{1,2} , Peter Sergeant ^{1,2,*} , Hendrik Vansompel ^{1,2}  and Tom Verstraten ³ ¹ Department of Electromechanical, Systems and Metal Engineering, Ghent University, 9000 Ghent, Belgium² FlandersMake@UGent—Corelab EEDT-MP, 3001 Leuven, Belgium³ Robotics and Multibody Mechanics Research Group (R&MM), Vrije Universiteit Brussel/Flanders Make, 1050 Brussels, Belgium

* Correspondence: peter.sergeant@ugent.be

Abstract: Powered prosthesis actuation is a field where energy efficiency and mass are important characteristics. The motion requirements of high torque at low speed and low torque at high speed are difficult to effectively combine in a single electric motor. A possibility is to use an oversized direct-drive motor that can deliver the peak torque. However, this results in a heavy actuation system and low overall efficiency. A common practice is combining a smaller electric motor with a gear reduction system. In the literature, novel redundant electric actuation systems have been presented with or without locking mechanisms to mitigate this problem. In this work, we provide a comparison of multiple electrical actuation systems composed of electric motors, gear reduction systems and locking mechanisms. This is done using the gait cycle of a human ankle as a case study. An electric motor with a double stator and a single rotor combined with a gearbox shows the most promising overall results when taking energy loss, total mass and complexity of the system into account.

Keywords: ankle gait cycle; high torque-low speed actuation; dual-motor actuation; optimization; finite-element; drivetrains; permanent magnet motor; legged locomotion; prosthesis actuation



Citation: Joos, Y.; Sergeant, P.; Vansompel, H.; Verstraten, T. Comparison of Drivetrain Topologies for an Ankle Gait Cycle. *Machines* **2023**, *11*, 23. <https://doi.org/10.3390/machines11010023>

Academic Editor: Jose Alfonso Antonino-Daviu

Received: 25 November 2022

Revised: 19 December 2022

Accepted: 20 December 2022

Published: 25 December 2022



Copyright: © 2022 by the authors. Licensee MDPI, Basel, Switzerland. This article is an open access article distributed under the terms and conditions of the Creative Commons Attribution (CC BY) license (<https://creativecommons.org/licenses/by/4.0/>).

1. Introduction

Powered prosthesis actuation is an active research area with ongoing research towards lightweight and energy efficient actuation systems. Actually, this can be extended to the field of legged locomotion and exoskeletons. Electric actuation systems are widely tested within this field. Electric motors have a long lifetime, low maintenance, robustness in operation and high energy efficiency around the nominal working point. Although the latter is true, the drive cycles within the prosthesis actuation field often combine the need for a high torque at low speed and a low torque at high speed. A motor can be efficiently designed to cover one of the two regions but this at the cost of poor efficiency in the other region [1]. This results in low overall efficiency over the drive cycle. To deliver the peak torque, large electric motors are often combined with gear reducers. However, this results in a heavy actuation system and low overall efficiency [2]. A common method to obtain a compact and relatively efficient drivetrain is by combining a smaller electric motor with a gear reduction system to reduce the motor torque requirement [3–7]. This is the most commonly used topology and therefore the reference topology of this study. A more recent topology is the dual-motor (redundant) actuation system [8–10]. This system combines two motors (or more) with different optimal working regions, e.g., a high torque-low speed motor and a low torque-high speed motor. The motors are mechanically combined to the output. This topology is also studied in the field of electric vehicles [11,12]. Electric motors which combine two rotors in one frame are receiving more and more attention [13–16]. These could be a compact solution for dual-motor actuation systems since the two motors can be combined in one package. Locking mechanisms are often used in redundant actuators to reduce energy consumption by selecting the most efficient actuator(s) while mechanically locking the other(s) [6,17,18]. Another electric motor trend is the use of a

motor with two stators and a common rotor [19,20]. This type of motor can obtain a higher torque density compared to an inner or outer rotor surface-mount permanent magnet motor [20]. In this work, these different options are compared to each other. First, the ankle gait cycle is introduced. The theoretical models of the topologies and the building blocks are presented. Furthermore, the basic and the extended comparison are explained. This is done in Section 2. Secondly, the results of the basic and the extended comparison are presented and discussed in Section 3. Finally, the conclusions of this study are found in Section 4.

2. Methods

2.1. Drive Cycle: Ankle Gait Cycle

The drive cycle corresponds to Winter's gait cycle of a human ankle for a person of 75 kg with a natural cadence [21]. Figure 1 shows the angle, angular velocity, torque and power of the ankle during a step. As can be seen, the ankle gait cycle can be classified as a high torque-low velocity drive cycle. The cycle has steep angle and torque variations. Most of the required ankle power is delivered during a fraction of the total ankle cycle period, see Figure 1d. The power peak is the push-off. The ankle gait cycle is characterised by two distinct phases. In the stance phase (first two thirds of the cycle), the ankle supports the full body weight, and ankle torque is relatively high. In the swing phase (final third of the cycle) the foot is lifted off the ground and torque is negligible.

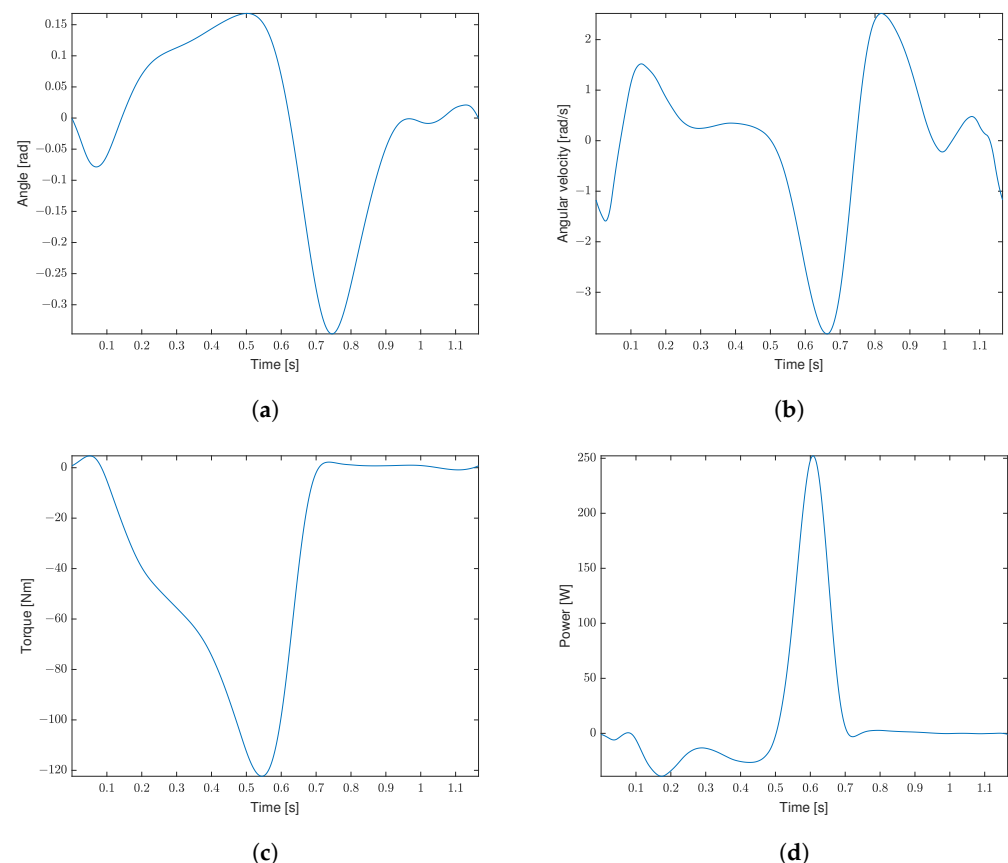


Figure 1. (a) Angle, (b) Angular velocity, (c) Torque and (d) Power of the ankle over the gait cycle.

2.2. Drivetrain Building Blocks: Modelling

The building blocks of the considered drivetrains are the (planetary) gearbox, the planetary differential, the electric motor and the brake (locking mechanism). The gearbox and the differential are modelled according to [10,22]. The electric motor will be modelled using the standard DQ0-modelling techniques. The brake is modelled as an ideal locking mechanism. The models will be briefly explained.

2.2.1. Gearbox

A simple way to model the (planetary) gearbox meshing losses, proposed in [23], is the efficiency function:

$$C_{PG} = \eta_{PG}^{-\text{sign}(T_o \cdot \omega_o)} \quad (1)$$

where T_o , ω_o & η_{PG} is the output torque, the output angular velocity and the planetary gearbox (PG) meshing efficiency, respectively. The meshing losses will result in a torque loss and therefore also a power loss during the transmission of power through the gearbox $P_{PG,l}$. This can be quantified according to:

$$\omega_o = \omega_i \cdot n_{PG} \quad (2)$$

$$T_o = C_{PG} \cdot \frac{T_i}{n_{PG}} \quad (3)$$

$$\begin{aligned} P_{PG,l} &= \omega_o * T_o - \omega_i * T_i \\ &= (C_{PG} - 1) * P_i \end{aligned} \quad (4)$$

with n_{PG} , ω_i and T_i the gear ratio, the input angular velocity and the input torque, respectively. The physical interpretation of the power loss model is the following. When power is delivered to the output (i.e., $T_o \cdot \omega_o > 0$), the efficiency function will be larger than one (i.e., $C_{PG} > 1$). Therefore, the loss during the power transfer through the gearbox is positive (i.e., $P_{PG,l} > 0$). So, power is lost during transmission from the input to the output side. When $T_o \cdot \omega_o < 0$, C_{PG} will be smaller than one. This results in a positive loss as expected. This time power is lost during transmission from the output to the input side.

2.2.2. Planetary Differential

The conceptual modelling of the planetary differential (PD) is similar to the modelling of the gearbox. The relation between the differential ratio ρ and the standard gearbox gear ratio n_{PG} is given by:

$$\rho = n_{PG} - 1 \quad (5)$$

Compared to the classical gearbox, the differential has three mechanical ports: ring, carrier and sun. There are multiple input-output combinations possible [18]. In this paper, the ring and the sun are the inputs while the carrier is the output. Due to the extra mechanical port of the system, an extra kinematic degree-of-freedom is present which results in a system of equations. A more detailed explanation can be found in [18,22]. Again an efficiency function is defined:

$$C_{PD} = \eta_{PD}^{-\text{sign}(T_c \cdot (\omega_s - \omega_c))} \quad (6)$$

where T_c , ω_s , ω_c & η_{PD} is the carrier branch torque, the sun branch angular velocity, the carrier branch angular velocity and the planetary differential meshing efficiency, respectively. The torque and speed relationship between the different branches is given by:

$$\begin{bmatrix} T_s \\ T_r \end{bmatrix} = \begin{bmatrix} 1 \\ C_{PD} \cdot \rho \\ 1 + C_{PD} \cdot \rho \end{bmatrix} \cdot T_c \quad (7)$$

$$\omega_c = \frac{1}{1 + \rho} \cdot \omega_s + \frac{\rho}{1 + \rho} \cdot \omega_r \quad (8)$$

with T_s , T_r and ω_r the sun branch torque, the ring branch torque and the ring branch angular velocity, respectively. The kinematic degree-of-freedom is visible in the planetary differential velocity constraint (Equation (8)).

2.2.3. Motor: Standard 3-Phase Modelling

The electric motor is modelled in the DQ0 reference frame. The transformation from the phase ABC to the DQ0 reference frame is given by the Park [24] and the power-variant Clarke [25] transformation. The zero-sequence component is left out due to a non-grounded wye connection. This gives the following state-space model in the DQ reference frame:

$$\begin{bmatrix} V_d \\ V_q \end{bmatrix} = \begin{bmatrix} R_s & -L_q \cdot \omega_e \\ L_d \cdot \omega_e & R_s \end{bmatrix} \cdot \begin{bmatrix} I_d \\ I_q \end{bmatrix} + \begin{bmatrix} L_d & 0 \\ 0 & L_q \end{bmatrix} \cdot \frac{d}{dt} \begin{bmatrix} I_d \\ I_q \end{bmatrix} + \begin{bmatrix} -\omega_e \cdot \Psi_{PM,q} \\ \omega_e \cdot \Psi_{PM,d} \end{bmatrix} \quad (9)$$

The subscript 'd' denotes the direct axis component and the subscript 'q' denotes the quadrature axis component. V , I , R_s , L and Ψ_{PM} denotes the voltage, the current, the stator resistance, the stator inductance and the permanent magnet induced coupled flux, respectively. ω_e is the electric angular velocity. The electromagnetic torque produced:

$$T_{em} = \frac{3}{2} \cdot N_p \cdot (\Psi_d \cdot I_q - \Psi_q \cdot I_d) \quad (10)$$

where N_p is the number of pole pairs. The total coupled fluxes Ψ are:

$$\Psi_d = \Psi_{PM,d} + L_d \cdot I_d \quad (11)$$

$$\Psi_q = \Psi_{PM,q} + L_q \cdot I_q \quad (12)$$

Field-oriented control is applied during this analysis. Therefore, the permanent magnet flux is oriented in the D-direction (i.e., $\Psi_{PM,d} \neq 0$ and $\Psi_{PM,q} = 0$) and only quadrature current is injected, i.e., $I_q \neq 0$ and $I_d = 0$.

2.2.4. Brake

The brake is used as a locking mechanism. Thus, the brake cannot be engaged when the axle is still rotating. This means that the axle will be brought to standstill by the motor on the axle through the concept of regenerative braking. Once the axle is brought to standstill, the brake can be engaged. The state of the brake can be modelled as:

$$\begin{cases} \delta_b = 1, \text{ Brake is closed/engaged} \\ \delta_b = 0, \text{ Brake is open/disengaged} \end{cases} \quad (13)$$

In order to not over complicate the analysis, the following assumptions are made:

- The static braking torque of the brake is higher than the load torque from the load cycle on the axle
- The reaction time of the brake is instantaneous
- The mass and the inertia are neglected
- The operating losses are neglected

In practice, the quantities of the above mentioned characteristics depend on the type of brake used [18].

2.3. Drivetrain Topologies

Multiple drivetrain topologies are compared to each other. These are introduced in this section.

2.3.1. Outrunner Motor and Gearbox

This is a common topology [26,27] and therefore the reference for the study. The permanent magnet rotor is connected to a gearbox. The output of the gearbox is connected to the ankle (i.e., the load), see Figure 2.

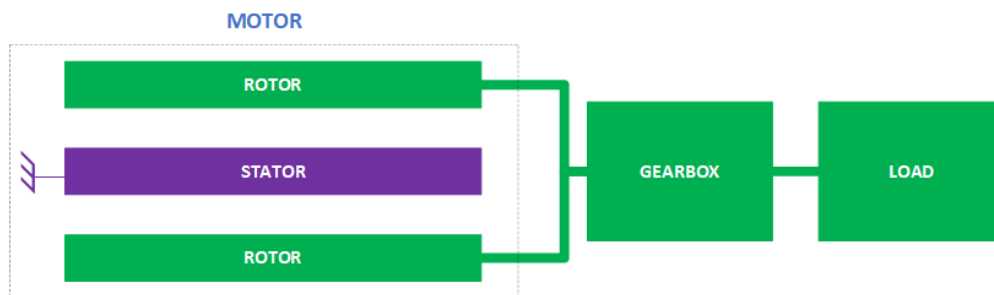


Figure 2. Topology 1: An electric motor, composed of one stator at the inside and one rotor at the outside, connected to the load via a gearbox.

This topology is abbreviated as “T1” for the remainder of this paper. The equation of motion at the motor side is given by:

$$(J_m + J_{PG,\rho} \cdot \frac{C_{PG}}{n_{PG}^2}) \cdot \frac{d\omega_m}{dt} = T_m - \frac{C_{PG} \cdot T_l}{n_{PG}} \tag{14}$$

where J , ω_m , T_m and T_l is the inertia, the rotor angular velocity, the torque acting on the rotor of the motor and the load torque, respectively. The subscript ‘o’ denotes the output side, i.e., side of the component closest to the load side. The subscript ‘m’ stands for motor. The torque balance of the electric motor is as follows:

$$T_{st} + T_m = 0 \tag{15}$$

with T_{st} the torque acting on the stator of the motor.

2.3.2. Dual-Motor, Differential and Gearbox

The electric motor is composed out of two rotors and two stators with a common iron yoke. The dual stator (i.e., outer and inner stator with common yoke) is located between the two rotors and is designed such that the common stator yoke is wide enough that the electric motor can be modelled as two independent motors, namely an out- and inrunner permanent magnet motor. The outer rotor is connected to the ring gear of the planetary differential, while the inner rotor is connected to the sun gear of the planetary differential. The output of the differential is connected to a gearbox. The output of the gearbox is connected to the ankle, see Figure 3.

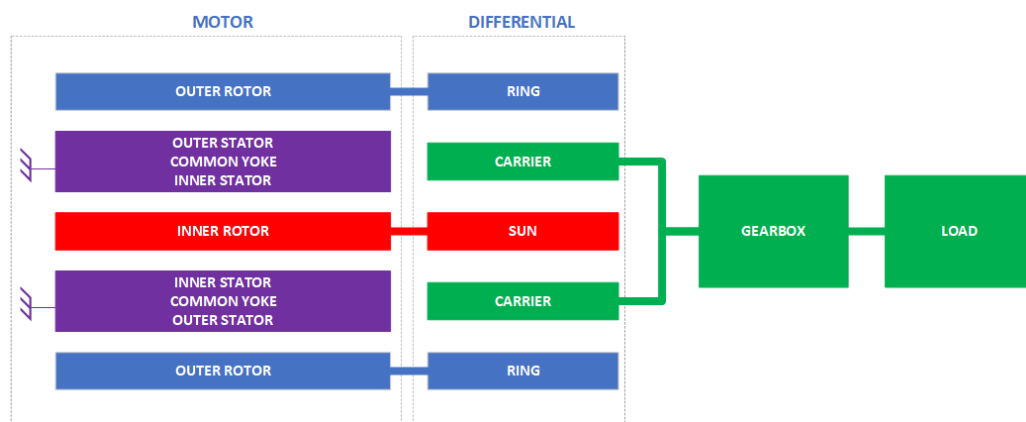


Figure 3. Topology 2: An electric motor, composed of one dual stator (i.e., outer and inner stator with common yoke) and two rotors surrounding the stator, connected to a differential. The differential is connected to the load via a gearbox.

This topology is abbreviated as “T2” for the remainder of this paper. The dynamic equation of motion at the motor side derived in [10] is used as a basis:

$$\mathbf{A} \cdot \frac{d\boldsymbol{\omega}_m}{dt} = \mathbf{T}_m - \mathbf{D} \cdot (T_l \cdot \frac{C_{PG}}{n_{PG}}) \quad (16)$$

where

$$\mathbf{T}_m = \begin{bmatrix} T_{m,s} \\ T_{m,r} \end{bmatrix} \quad (17)$$

$$\boldsymbol{\omega}_m = \begin{bmatrix} \omega_{m,s} \\ \omega_{m,r} \end{bmatrix} \quad (18)$$

$$\mathbf{A} = \begin{bmatrix} J_{m,s} + J_{PD,s} & 0 \\ 0 & J_{m,r} + J_{PD,r} \end{bmatrix} + (J_{PD,c} + J_{PG,o} \cdot \frac{C_{PG}}{n_{PG}^2}) \cdot \mathbf{D} \cdot \mathbf{J} \quad (19)$$

$$\mathbf{D} = \begin{bmatrix} \frac{1}{\rho \cdot C_{PD} + 1} \\ \frac{\rho \cdot C_{PD}}{\rho \cdot C_{PD} + 1} \end{bmatrix} \quad (20)$$

$$\mathbf{J} = \begin{bmatrix} \frac{1}{\rho + 1} & \frac{\rho}{\rho + 1} \end{bmatrix} \quad (21)$$

where \mathbf{T}_m , $\boldsymbol{\omega}_m$, \mathbf{A} , \mathbf{D} and \mathbf{J} represent the motor torque vector, the motor angular velocity vector, the inertia matrix, the differential torque distribution vector and the differential velocity weight vector, respectively. The meaning of the symbols in the matrices is the same as defined in Section 2.3.1. The subscripts ‘s’, ‘r’ and ‘c’ denote the sun branch, the ring branch and the carrier branch, respectively. The torque balance of the electric motor is as follows:

$$(T_{st,s} + T_{st,r}) + T_{m,s} + T_{m,r} = 0 \quad (22)$$

with $T_{st,s}$, $T_{st,r}$, $T_{m,s}$ and $T_{m,r}$ the torque of the stator facing the inner rotor, the torque of the stator facing the outer rotor, the torque of the inner rotor and the torque of the outer rotor, respectively. Furthermore, since the motor can be modeled as two independent motors Equation (22) can be decomposed:

$$T_{st,s} + T_{m,s} = 0, \text{ (inner rotor branch)} \quad (23)$$

$$T_{st,r} + T_{m,r} = 0, \text{ (outer rotor branch)} \quad (24)$$

2.3.3. Dual-Motor, Brakes, Differential and Gearbox

This topology is an extension of the previous topology T2. Brakes are added in the ring and sun branch, see Figure 4. They are located between the motor and the differential.

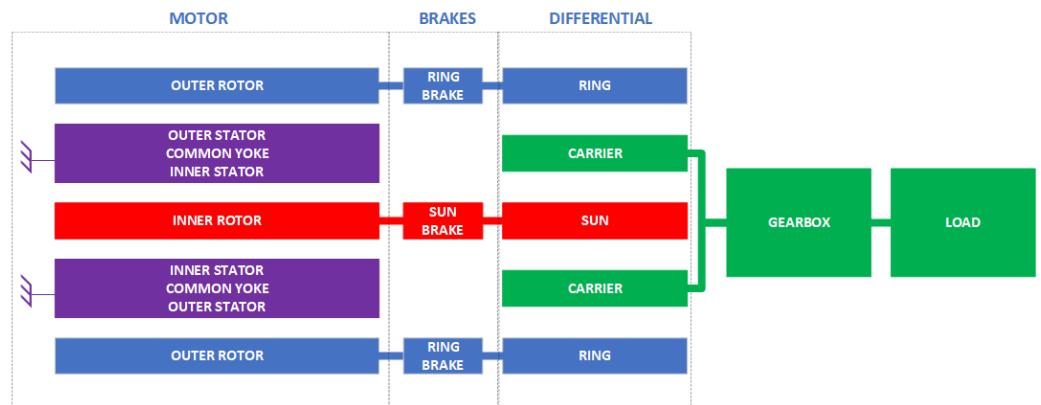


Figure 4. Topology 2.b: Variant of topology T2 with brakes added in the ring and sun branch.

Due to the similarity to topology T2, this topology is abbreviated as “T2.b” for the remainder of this paper. The dynamics are similar to topology T2. The only difference is the addition of the brake function matrix Δ_b :

$$\mathbf{A} \cdot \frac{d\Delta_b \cdot \omega_m}{dt} = \mathbf{T}_m - \Delta_b \cdot \left[\mathbf{D} \cdot \left(T_l \cdot \frac{C_{PG}}{n_{PG}} \right) \right] \quad (25)$$

where Equations (17)–(21) is still applicable with the addition of the braking function matrix:

$$\Delta_b = \begin{bmatrix} 1 - \delta_{b,s} & 0 \\ 0 & 1 - \delta_{b,r} \end{bmatrix} \quad (26)$$

with $\delta_{b,s}$ and $\delta_{b,r}$ the sun and the ring braking function defined as Equation (13), respectively. The torque balance equation is given by Equation (22) which can again be decomposed as Equations (23) and (24).

2.3.4. Dual-Motor, Gearbox and Flywheel

The electric motor is composed of a stator and two rotors. The outer rotor is a permanent magnet rotor while the inner rotor contains a 3-phase winding to generate a torque. The outer rotor is connected to the gearbox. The inner rotor is connected to a flywheel, see Figure 5.

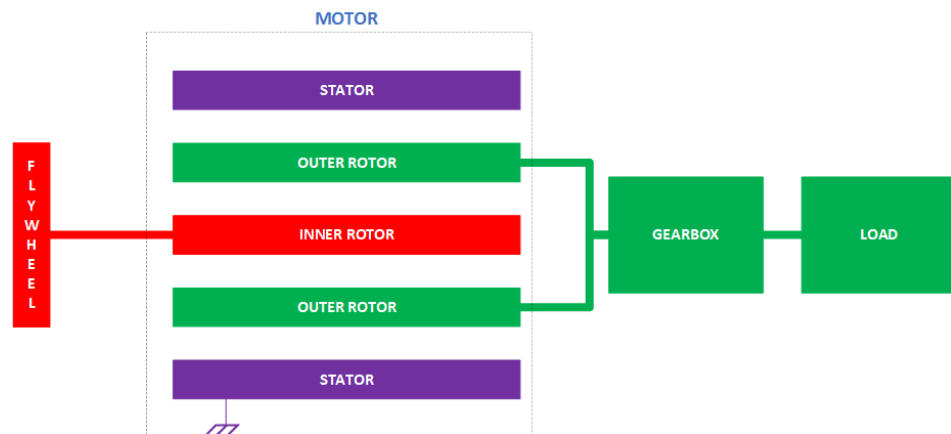


Figure 5. Topology 3: An electric motor composed of two rotors, one at the inside (inner rotor) and one in the middle (outer rotor) of the motor, and one stator. The inner rotor is connected to a flywheel. The outer rotor is connected to the load via a gearbox.

The output of the gearbox is connected to the ankle. This topology is abbreviated as “T3” for the remainder of this paper. The equation of motion at the motor side:

$$\mathbf{A} \cdot \frac{d\omega_m}{dt} = \mathbf{T}_m - \mathbf{D}^T \cdot \left(T_l \cdot \frac{C_{PG}}{n_{PG}} \right) \quad (27)$$

where

$$\mathbf{T}_m = \begin{bmatrix} T_{m,ir} \\ T_{m,or} \end{bmatrix} \quad (28)$$

$$\omega_m = \begin{bmatrix} \omega_{m,ir} \\ \omega_{m,or} \end{bmatrix} \quad (29)$$

$$\mathbf{A} = \begin{bmatrix} J_{m,ir} + J_f & 0 \\ 0 & J_{m,or} + J_{PG,o} \cdot \frac{C_{PG}}{n_{PG}^2} \end{bmatrix} \quad (30)$$

$$\mathbf{D} = \begin{bmatrix} 0 & 1 \end{bmatrix} \quad (31)$$

Equations (28)–(30) has the same meaning as Equations (17)–(19). The subscripts ‘*ir*’, ‘*or*’ and ‘*f*’ represent the inner rotor branch, the outer rotor branch and the flywheel, respectively. The vector **D** now represent the connection of the rotors to the gearbox. The torque balance of the electric motor is as follows:

$$T_{st} + T_{m,ir} + T_{m,or} = 0 \quad (32)$$

with T_{st} , $T_{m,ir}$ and $T_{m,or}$ the torque acting on the stator, the inner rotor and the outer rotor, respectively.

2.3.5. Dual-Stator and Gearbox

The electric motor is composed of two stators with a permanent magnet rotor in-between. The rotor is connected to the gearbox. The output of the gearbox is connected to ankle, see Figure 6.

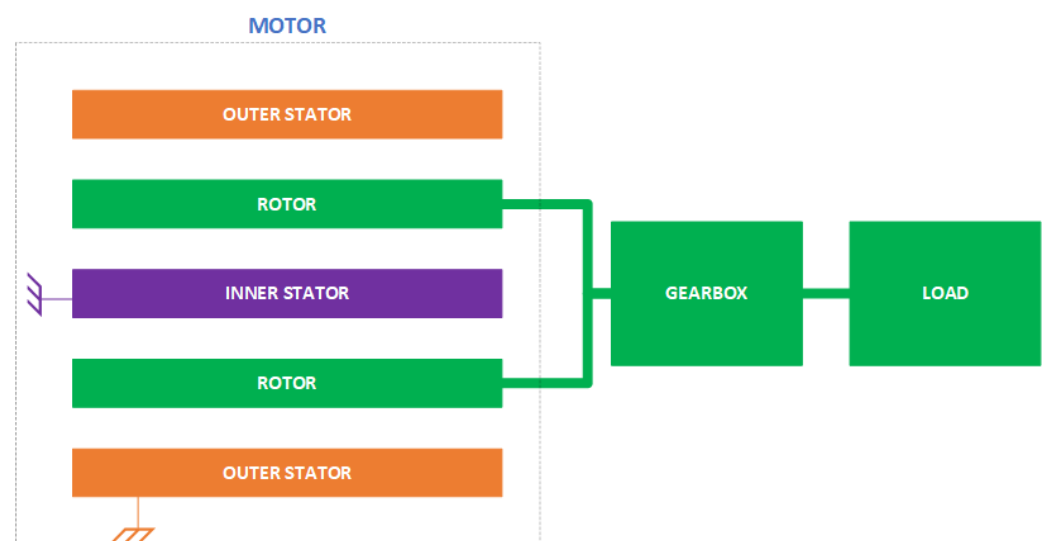


Figure 6. Topology 4: An electric motor composed of two stators, one at the inside (inner stator) and one at the outside (outer stator) of the motor, and one rotor connected to the load via a gearbox.

This topology can be seen as the case where for topology T3, the inner rotor is blocked. This topology is abbreviated as “T4” for the remainder of this paper. The dynamic equation of motion at the motor side is identical to that of topology T1:

$$(J_m + J_{PG,o} \cdot \frac{C_{PG}}{n_{PG}^2}) \cdot \frac{d\omega_m}{dt} = T_m - \frac{C_{PG} \cdot T_l}{n_{PG}} \quad (33)$$

The torque balance of the electric motor is as follows:

$$T_{st,i} + T_m + T_{st,o} = 0 \quad (34)$$

with $T_{st,i}$, T_m and $T_{st,o}$ the inner stator torque, the rotor torque and the outer stator torque, respectively.

2.3.6. Remarks

1. The Coulomb and viscous friction terms are difficult to estimate theoretically so typically they are identified through empirical means. Therefore, the Coulomb and viscous friction parts are omitted in this work.
2. Due to the nature of the load (closed cycle), the following must hold for all topologies:
 - A closed kinematic cycle for every branch, i.e., a closed angle cycle $\theta_{start} = \theta_{end}$, a closed angular velocity cycle $\omega_{start} = \omega_{end}$ and a closed angular acceleration cycle $\alpha_{start} = \alpha_{end}$

2.4. Basic Comparison

In this section, the different topologies are compared based on the mechanical characteristics of the motion. The drivetrain is assumed to be ideal during this section which means (if present in the topology):

- No meshing losses in the gearbox: $C_{PG} = 1$
- No meshing losses in the differential: $C_{PD} = 1$

For the basic comparison, the gearbox ratio n_{PG} and the differential ratio ρ if present was fixed to 40 and 9, respectively. For high torque-low speed application, the copper loss is the dominating loss since the copper loss is related to the square of the delivered torque. Therefore, the topologies are evaluated according to the proposed cost functions in Table 1.

Table 1. Cost functions.

Topology	Cost Function
T1	$\int_0^{T_{cycle}} (T_{st}^2) dt$
T2 & T2.b	$\int_0^{T_{cycle}} (T_{st,s}^2 + T_{st,r}^2) dt$
T3	$\int_0^{T_{cycle}} (T_{st}^2 + T_{m,ir}^2) dt$
T4	$\int_0^{T_{cycle}} (T_{st,i}^2 + T_{st,\rho}^2) dt$

In the basic comparison, the maximum delivered torque and angular velocity are limited to a realistic value for the considered application:

- Maximum torque delivered by an individual stator: $T_{max} = 10 \text{ Nm}$
- Maximum angular velocity of a rotor: $\omega_{max} = 500 \text{ rad/s}$

The cost function is evaluated for different orders of the reflected inertia to the rotor in each branch. For topologies T2, T2.b, T3 and T4, there is a degree of freedom. For T2 and T2.b, the output velocity does not completely determine the velocity of the branches. This can be seen in Equation (8). Therefore, the velocity of either the sun or the ring branch can be chosen freely. For T3, this is the torque distribution between the inner wound rotor and the stator due to the interaction torque within the motor (Equation (32)). However, this degree of freedom is limited due to the fact that the inner rotor-flywheel branch makes a closed cycle. Therefore, the net torque over a cycle, i.e., the torque obtained by integrating the instantaneous torque over one cycle, delivered by the inner rotor must be zero. For T4, this is the torque distribution between the two stators. Compared to topology T3, the inner stator is mechanically locked and therefore the net torque delivered over a cycle can be different from zero. This enables torque profiles which are not possible for topology T3. An optimal choice for the degree-of-freedom for the three topologies T2, T3 and T4 is found through an optimization. The degree of freedom ($f(x)$) is approximated by a finite Fourier series of dimension N :

$$f(x) \approx \frac{a_0}{2} + \sum_{n=1}^N a_n \cdot \cos\left(\frac{n \cdot \pi \cdot x}{L}\right) + \sum_{n=1}^N b_n \cdot \sin\left(\frac{n \cdot \pi \cdot x}{L}\right) \quad (35)$$

where L is equal to half the cycle period. During every iteration of the optimization, the optimizer delivers the Fourier serie coefficients. Using the dynamic equations and relationships presented in the previous section, the other unknown quantities are calculated. As for topology T2, topology T2.b has a kinematic degree-of-freedom. Additionally, the brakes add an extra decision namely to disengage both brakes or to disengage one of the two brakes and engage the other brake. The opening and closing of the brakes introduces a discontinuity into the system. Therefore, instead of a finite dimensional Fourier series, the ankle gait cycle is discretized using K discretization points and I_b braking intervals

are introduced. At every discretization point, a value for the velocity is given, taking into account the braking state present at that point. During a braking interval, the brakes are kept in the desired state. During the transition from one braking interval to the next, the braking state can be modified. This strategy is similar to the strategy used in [17]. A brute-force search is employed to make sure that all possible braking solutions are checked. Due to the exponential relationship between the number of braking intervals and the total amount of simulations, the number of intervals is limited, see Table 2. The braking intervals used for our analysis are shown in Figure 7.

Table 2. Discretization parameters for topology T2.b for the basic comparison.

Name	Symbol	Value	Unit
Number of discretization points	K	241	-
Number of braking intervals	I_b	8	-

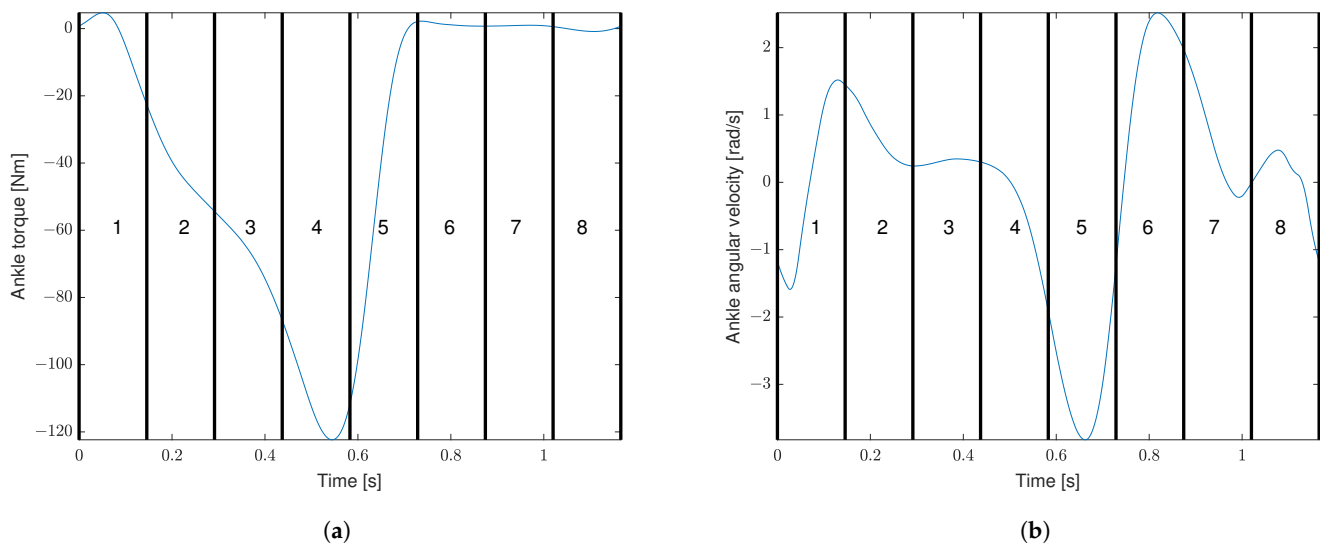


Figure 7. Braking interval placement over the cycle (a) Ankle torque (b) Ankle angular velocity.

2.5. Extended Comparison

The basic analysis of the previous section is extended. The following topologies are considered in this section: T1, T2, T2.b and T4. As will be shown in Section 3.1, topology T3 has a worse performance compared to topology T4 due to the closed kinematic cycle constraint. Since topology T3 and T4 are very similar (see Section 2.4), the best performing of the two is kept which is topology T4. The topologies are compared in the following way. For topology T2 and T2.b, the optimizer is allowed to choose the axial length and the cross-sectional parameters of the motor. The active motor masses (i.e., the motor mass without the mass of the end-windings) of the obtained Pareto points are extracted. For each active motor mass, the optimization of topology T1 and T4 is done given the active mass as a constraint. This is obtained through axial scaling of the cross-sectional area. The parameters of the cross-sectional area are free to be chosen by the optimizer within the dimensional space limits. The losses of the drivetrain, i.e., gearbox and/or differential losses, and the electric motor, i.e., copper and iron losses, are included in the analysis. The electric motor and the drivetrain are optimized to the ankle cycle such that the best results of the different topologies can be compared. The criteria are the losses over the cycle and the total topology mass.

2.5.1. General Constraints

The general constraints applying to all the topologies in the extended comparison can be found in Table 3. A maximum RMS current density limit of 5 A/mm² is chosen according to [28] for a small, naturally air-cooled permanent magnet motor.

Table 3. General constraints applied to all considered topologies in the extended comparison.

Name	Symbol	Value	Unit
DC-voltage	V_{DC}	48	V
Maximum outer diameter	$D_{o,max}$	140	mm
Minimum inner diameter	$D_{i,min}$	10	mm
Maximum axial length	$l_{axial,max}$	100	mm
Gearbox gear ratio range	n_{PG}	[1, 50]	-
Differential ratio range	ρ	[1, 9]	-
Maximum RMS current density	$J_{rms,max}$	5	A/mm ²

2.5.2. Finite-Element Models of the Motors

The electric motors of the different topologies share the following parameters (Table 4):

Table 4. General FEMM parameters.

Name	Symbol	Value	Unit
Number of phases	N_{ph}	3	-
Number of slots	N_{slots}	24	-
Number of pole pairs	N_p	10	-
Permanent magnet remanent magnetic flux density	B_r	1.17	T
Permanent magnet relative permeability	$\mu_{r,PM}$	1.05	-
Copper conductors conductivity at 20 °C	$\sigma_{Cu,20}$	58	MS/m
Resistive temperature coefficient of copper	α_{Cu}	0.393	%/°C
Airgap width	δ_{air}	0.5	mm

The chosen pole-slot combination has a high fundamental winding factor. Furthermore, the iron yoke can be reduced with an increasing number of pole pairs. The magnetic iron core material is NO20 electric steel. This core material is used for all the magnetic core parts, i.e., the stator and the rotor. The only exception is the sleeve of the rotor of topology 4. This sleeve is made of non-magnetic stainless steel (grade 316) and has the function to hold and fixate the magnets. The density of the used materials are given in Table 5.

Table 5. Material mass density information.

Material	Value	Unit
Copper	8960	kg/m ³
NO20	7650	kg/m ³
NdFeB magnet	7700	kg/m ³
Non-magnetic stainless steel (grade 316)	8000	kg/m ³

The winding layout for all topologies is a double-layer fractional-slot concentrated winding. Concentrated windings have some advantages compared to distributed windings for low-speed applications like shorter end-windings, low cogging torque, good fault-tolerant capabilities, lower mutual coupling between phases, ... [29,30]. The harmonic content in the magnetic field and thus the back-emf is typically higher for concentrated windings compared to distributed windings which results in higher magnetic losses [30–32]. A double-layer has a lower torque ripple, harmonic content, eddy current losses and end-windings compared to single-layer windings. However, the fundamental winding factor and overload torque capability decreases slightly [29]. However, this is only a problem in

high-speed applications which is not the application of this paper. A cross-sectional view of the different topologies can be seen in Figure 8. The meaning of the parameters withing the figure can be found in Table 6.

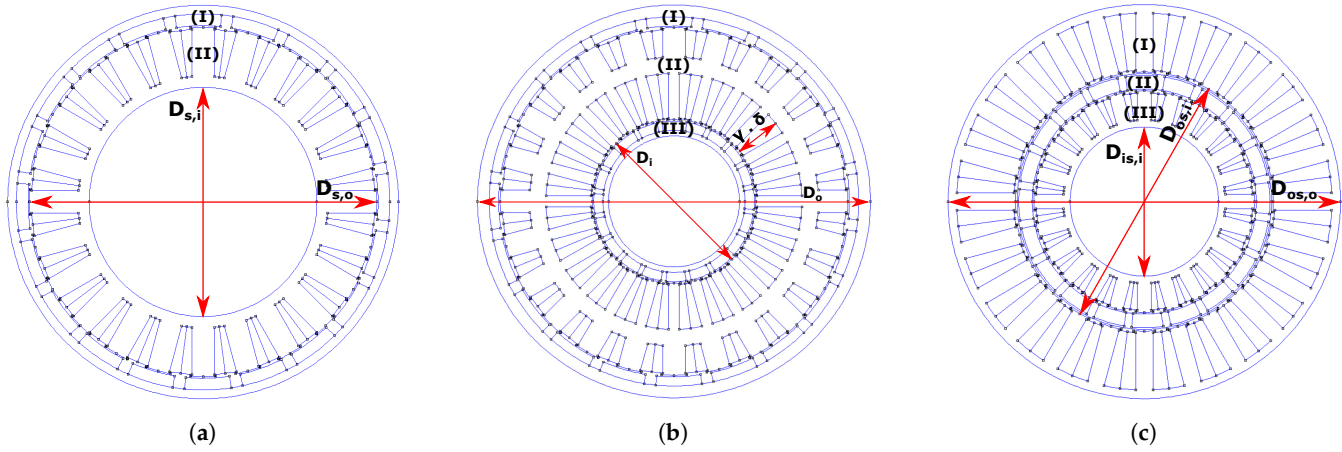


Figure 8. Cross-sectional view of the motor (a) Topology T1: (I) and (II) are the outer rotor and stator, respectively. (b) Topology T2 & T2.b: (I), (II) and (III) are the outer rotor, dual stator (i.e., outer and inner stator with common yoke) and inner rotor, respectively. (c) Topology T4: (I), (II) and (III) are the outer stator, rotor and inner stator, respectively.

Table 6. Inputs for the forward neural network to estimate the no-load flux for a given cross-sectional geometry of the motor for the respective topologies.

Topology	Name	Symbol
T1	Stator outer diameter	$D_{s,o}$
	Stator inner diameter	$D_{s,i}$
T2 & T2.b	Outer diameter	D_o
	Inner diameter	D_i
	Slot fraction factor	γ
T4	Outer stator outer diameter	$D_{os,o}$
	Outer stator inner diameter	$D_{os,i}$
	Inner stator inner diameter	$D_{is,i}$

The only parameter that is not found in this table is the available radial space for the stator slots δ . This parameter is found by back-calculation of the geometry starting from the parameters in Table 6 and using the relationships given below. The slot fraction factor γ gives the radial slot space given to the inner sided stator. The allowed range of γ is [0.2, 0.8].

Figure 9 shows the geometry of the stator tooth and the magnet rotor. The quantities have the following values for all the topologies:

- Pole pitch: $\tau_p = \frac{2 \cdot \pi}{2 \cdot N_p}$
- Slot pitch: $\tau_s = \frac{2 \cdot \pi}{N_{slots}}$
- The ratio of the magnet width to the pole pitch: $\frac{\tau_m}{\tau_p} = 0.8 = \alpha_{PM}$
- The tooth width is half the slot width: $\tau_t = \tau_s / 2$
- The stator yoke width is half the tooth width: $h_{ys} = \tau_t / 2$
- The permanent magnet rotor yoke height [28] (chapter 3):

$$h_{yr} = \frac{\alpha_{PM} \cdot \hat{B}_\delta \cdot \tau_p}{2 \cdot k_{Fe} \cdot \hat{B}_{yr}} \quad (36)$$

with \hat{B}_δ , k_{Fe} and \hat{B}_{yr} the magnetic flux density amplitude in the airgap (typically 1 T), the space factor of the iron and the magnetic flux density saturation amplitude in the rotor iron yoke (typically 1.7–1.8 T), respectively. For topology T4, the yoke has a height of 0.5 mm since it only serves to support and fixate the magnets.

- The permanent magnet rotor magnet height [28] (chapter 3):

$$h_m = \frac{\delta_{air} \cdot \hat{B}_\delta \cdot \mu_{r,PM}}{B_r - \hat{B}_\delta} \quad (37)$$

with δ_{air} the airgap width. For topology T4, the height of the permanent magnet was fixed to 4 mm since the double airgap around the rotor would otherwise result in too much permanent magnet mass.

- Fixed: $l_t = 0.25$ mm, $l_b = 0.5$ mm and $\alpha = 30^\circ$.

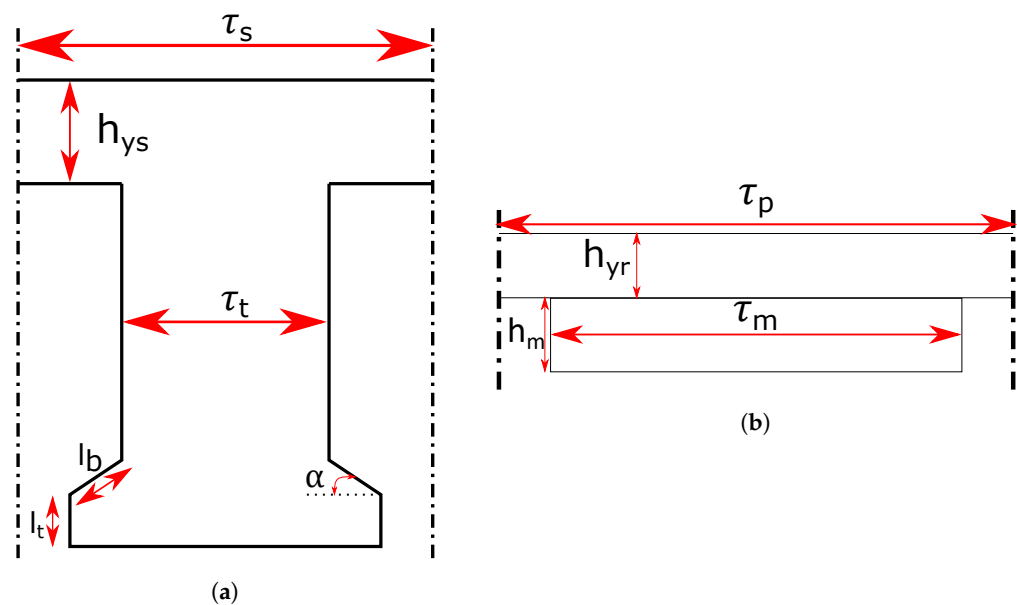


Figure 9. (a) Stator tooth geometry (one slot pitch). (b) Permanent magnet rotor geometry (one pole pitch).

2.5.3. Flux Variation under Current Loading

Due to the Q-direction current injection to deliver the required torque, the D-direction coupled flux can decrease as a result of cross-saturation. This influence is studied by taking a design for the three different motor models, see Figure 8, and looking at the D-direction coupled flux under no-load, i.e., no current injection, and a certain injected Q-direction current density. The rotor is positioned such that the a-phase axis aligns with the D-direction. The maximum allowed RMS current density is 5 A/mm² (Table 3). Assuming a sinusoidal current injection waveform, the amplitude and thus the maximum instantaneous injected Q-direction current density is 7.071 A/mm². The amplitude of the coupled flux vector is also calculated according to:

$$\hat{\Psi} = \sqrt{\Psi_D^2 + \Psi_Q^2} \quad (38)$$

The simulations are done using the finite-element software “FEMM”. The results are shown in Tables 7–9 for topology T1, T2/T2.b and T4, respectively. It can be concluded that the influence of the injected Q-direction current on the D-direction coupled flux is very small. There is little difference between the coupled flux amplitude for no-load and under current loading. Notice that the no-load coupled flux amplitude and the no-load D-direction coupled flux are equal. Only the permanent magnets are generating a magnetic field during no-load and these are oriented in the D-direction. Therefore, the no-load flux

can be used in the optimization with a very small loss of accuracy. The influence of one stator part on the other stator part, e.g., the inner stator on the outer stator, is very small for topology T2/T2.b (Table 8) and topology T4 (Table 9).

Table 7. D-direction coupled flux [Wb] (Ψ_D) and coupled flux amplitude [Wb] ($\hat{\Psi}$) for no-load and Q-direction current density injection for topology T1 ($D_{s,o} = 56.18$ mm, $D_{s,i} = 26.45$ mm and $l_{axial} = 25.19$ mm).

$\hat{J}_{Cu,st}$ [A/mm ²]	0	7.071
Ψ_D [Wb]	2.13723×10^{-3}	2.13566×10^{-3}
$\hat{\Psi}$ [Wb]	2.13723×10^{-3}	2.14490×10^{-3}

Table 8. D-direction coupled flux [Wb] (indicated by the subscript ‘D’) and coupled flux amplitude [Wb] (indicated by the subscript ‘A’) for no-load and Q-direction current density injection for topology T2/T2.b ($D_o = 60.23$ mm, $D_i = 19.14$ mm, $\gamma = 0.4875$ and $l_{axial} = 23.16$ mm). The first value of the pair is the outer stator result and the second value of the pair is the inner stator result, i.e., ($\Psi_{outer\ stator}, \Psi_{inner\ stator}$).

$\hat{J}_{Cu,st,r}$ [A/mm ²]	$\hat{J}_{Cu,st,s}$ [A/mm ²]	0	7.071
0		$(1.89228 \times 10^{-3}, 8.27981 \times 10^{-4})_D$	$(1.89228 \times 10^{-3}, 8.27669 \times 10^{-4})_D$
		$(1.89228 \times 10^{-3}, 8.27981 \times 10^{-4})_A$	$(1.89228 \times 10^{-3}, 8.3431 \times 10^{-4})_A$
7.071		$(1.89205 \times 10^{-3}, 8.27982 \times 10^{-4})_D$	$(1.89205 \times 10^{-3}, 8.27670 \times 10^{-4})_D$
		$(1.89483 \times 10^{-3}, 8.27981 \times 10^{-4})_A$	$(1.89483 \times 10^{-3}, 8.34313 \times 10^{-4})_A$

Table 9. D-direction coupled flux [Wb] (indicated by the subscript ‘D’) and coupled flux amplitude [Wb] (indicated by the subscript ‘A’) for no-load and Q-direction current density injection for topology T4 ($D_{os,o} = 55.01$ mm, $D_{os,i} = 35.05$ mm, $D_{is,i} = 17.87$ mm and $l_{axial} = 34.73$ mm). The first value of the pair is the outer stator result and the second value of the pair is the inner stator result, i.e., ($\Psi_{outer\ stator}, \Psi_{inner\ stator}$).

$\hat{J}_{Cu,st,o}$ [A/mm ²]	$\hat{J}_{Cu,st,i}$ [A/mm ²]	0	7.071
0		$(1.47909 \times 10^{-3}, 1.43967 \times 10^{-3})_D$	$(1.47909 \times 10^{-3}, 1.43962 \times 10^{-3})_D$
		$(1.47909 \times 10^{-3}, 1.43967 \times 10^{-3})_A$	$(1.47910 \times 10^{-3}, 1.44083 \times 10^{-3})_A$
7.071		$(1.47885 \times 10^{-3}, 1.43962 \times 10^{-3})_D$	$(1.47885 \times 10^{-3}, 1.43960 \times 10^{-3})_D$
		$(1.52517 \times 10^{-3}, 1.43998 \times 10^{-3})_A$	$(1.52678 \times 10^{-3}, 1.44249 \times 10^{-3})_A$

2.5.4. No-Load Flux Response Surface

In order to speed-up the optimization, the no-load flux, which will be used to estimate the electromagnetic torque, the iron losses and the back-emf, is approximated using a response surface. During no-load, only the permanent magnets generate a magnetic field. The rotor is positioned such that the a-phase axis aligns with the D-direction. Therefore, only the D-direction of the coupled flux needs to be approximated since the Q- and 0-direction coupled flux will be very close to zero. By the use of a response surface model, the time-expensive finite element simulations are saved during the optimization. In order to generate the response surface, finite-element simulations are required. The training points are generated through a constrained Latin hypercube sampling method which takes the geometric and thus physical constraints of the parameters into consideration, e.g., the stator and the rotor cannot overlap, ... The finite-element simulations are done using the finite-element software ‘‘FEMM’’. The response surface is a forward neural network model

with one hidden layer. For each topology, multiple neural networks with a different amount of neurons ranging from 4 to 20 are fitted. The best performing network, i.e., the lowest bias and variance compared to the test data points, is selected. The accuracy of the selected network for each topology is shown in Figure 10. The parameters which are used as inputs for the neural network for each topology can be found in Table 6.

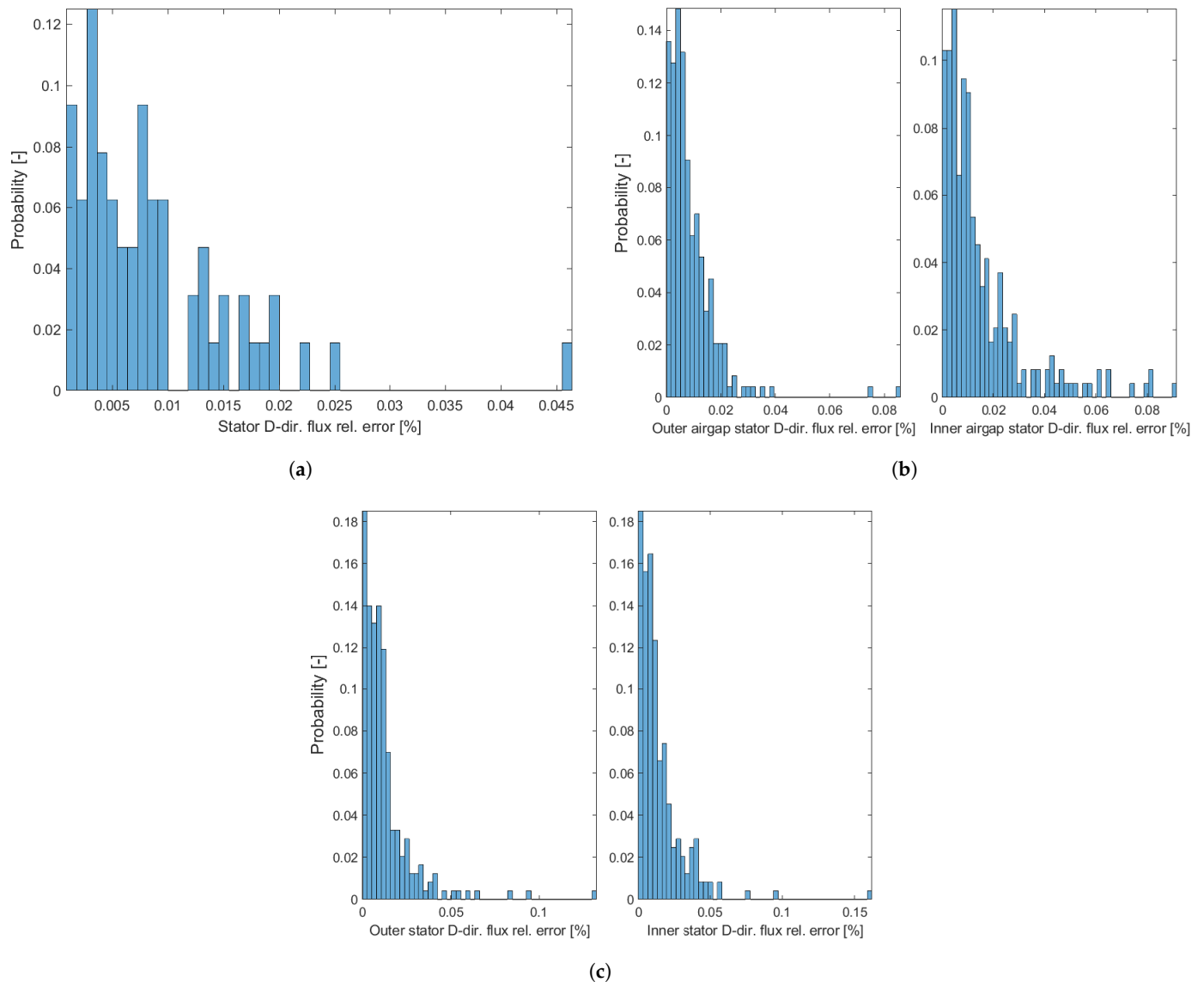


Figure 10. Forward neural network D-direction coupled flux relative error (a) Topology T1: 18 neurons (b) Topology T2 and T2.b: 20 neurons (c) Topology T4: 12 neurons.

2.5.5. Mass and Inertia

Inertia is important when evaluating the performance over a dynamic cycle. The mass and the inertia of connection parts like axles etc where not considered during the simulation.

Gearbox and Differential

The Neugart PFLE gearbox datasheet data is used during this study to obtain the mass and the inertia of the gearbox. As was mentioned earlier, a gearbox can be transformed in a differential. The inertia of the different parts within the differential, i.e., the ring, sun and carrier inertia cannot be found directly within the datasheet given by the manufacturer. These are estimated using the method given in [33]. Multiple sizes are available where the mechanical strength but also the mass and the inertia increases with the size. The

mass remains constant with changing gear ratio for gearboxes of the same size. On the contrary, the inertia changes with the gear ratio even if the size is kept constant. The mechanical loading (i.e., the torque transmitted) will be checked during the optimization and the appropriate size (i.e., the smallest size able to fulfill the torque requirement) will be selected. The gearboxes in the drivetrain are 1-stage (up to a ratio of 10) or 2-stage (limited during simulation to a ratio of 50). The differential of topology T2 and T2.b is constructed from a Neugart PFLE gearbox. Since the differential ratio is limited to 9. The differential is a single-stage differential. The datasheet of the considered gearbox contains a limited number of gear ratios between the considered gear ratio limits. During the optimization presented in Section 2.5.8, linear interpolation is employed to obtain the inertia for gear ratios not present in the datasheet.

Motor

The inertia of the motor is calculated using analytical formulas through the decomposition into cylindrical segments. The mass was also analytically calculated based on the volume of every material used in the motor. This includes the end-windings.

2.5.6. Gearbox and Differential Efficiency

In order to account for the absence of the friction terms, the efficiency used in the simulation is lower than the efficiency found in the datasheet. The efficiency of a gearbox is strongly dependent on the number of stages and less on the gear ratio variation over a specific stage itself [23]. For this reason, the efficiency for a specific amount of stages is kept constant over the gear ratio range. A gearbox ratio of one is possible. This corresponds physically with a direct connection between the input and the output. Therefore the efficiency for a gearbox ratio of one is 100%. Note that a differential ratio ρ corresponds with a gearbox ratio of $\rho + 1$ (Equation (5)) and that only single-stage differentials are considered. According to Table 10, the differential always has an efficiency of 90% when present.

Table 10. Gearbox and differential efficiency as function of number of stages.

Number of Stage	Gearbox Ratio	Efficiency
1	[2, 10]	90%
2	[11, 50]	80%

2.5.7. Losses

Drivetrain Losses

The drivetrain losses or mechanical losses are given by the efficiency function of the planetary gearbox and the differential if present in the considered drivetrain topology. The mechanical energy loss over the ankle gait cycle is given by:

$$E_{l,mech} = \int_0^{T_{cycle}} (P_{mech,in} - P_{mech,out}) dt \quad (39)$$

where $P_{mech,in}$ and $P_{mech,out}$ stands for the mechanical power given to and taken from the system, respectively. $P_{mech,out}$ is the demanded ankle power, see Figure 1d. $P_{mech,in}$ for the considered topologies in the extended comparison can be found in Table 11.

Table 11. Mechanical power input $P_{mech,in}$ formulas.

Topology	$P_{mech,in}$
T1	$T_m * \omega_m$
T2 & T2.b	$T_{m,s} * \omega_{m,s} + T_{m,r} * \omega_{m,r}$
T4	$T_m * \omega_m$

Electric Motor Losses

The losses of the electric machine are composed of the copper losses and the iron losses. The copper losses are calculated using:

$$P_{Cu} = 3 \cdot R \cdot I^2 \quad (40)$$

where I is the effective value of the phase current. The phase resistance R is calculated assuming a temperature of 100 °C during the cycle and a serie connection between the phase slots [28]. The iron loss density is calculated using the commonly used model of decomposing the iron loss in a hysteresis, eddy current and excessive part (see Section 5.5.3 of [15]):

$$\begin{aligned} P_{Fe} &= P_h + P_e + P_{ex} \\ &= a \cdot \hat{B}^\alpha \cdot f + b \cdot \hat{B}^2 \cdot f^2 \\ &\quad + c \cdot \hat{B} \cdot f \cdot \left(\sqrt{1 + d \cdot \hat{B} \cdot f} - 1 \right) \end{aligned} \quad (41)$$

where the parameters a , b , c , d and α are material specific coefficients. \hat{B} is the amplitude of the magnetic flux density in the iron part and f is the frequency of the magnetic field density waveform. The iron losses are calculated separately in the iron tooth and yoke since these typically have a different magnetization level. The B-field in the two parts are estimated using the method described in Section 5.5.3 of [15]. The total motor energy loss over the drive cycle is given by:

$$E_{l,motor} = \int_0^{T_{cycle}} (P_{Cu,t} + P_{Fe,t}) dt \quad (42)$$

where $P_{Cu,t}$ and $P_{Fe,t}$ stands for the total copper loss and the iron loss of the motor, respectively.

2.5.8. Optimization Procedure

As explained earlier (Section 2.5), the comparison starts by first finding the Pareto front for topology T2 and T2.b. The Pareto front for topology T2 and T2.b is obtained through the optimization procedure shown in Figure 11b. The design is a multi-objective optimization with as objectives: the total mass of the topology (i.e., mass of the motor, gearbox and differential) and the losses over one load cycle. The multi-objective optimization algorithm gives a new design point consisting of the cross-sectional parameters of topology T2 (see Table 6), the axial length of the motor l_{axial} , the gearbox ratio n_{PG} and the differential ratio ρ . The high-level mathematical representation for the procedure is shown in Figure 11b is as follows:

$$\mathbf{x}^* = \min_{\mathbf{x} \in \mathbf{X}} \left(E_{l,mech} + E_{l,motor}, m_{motor} + m_{PG} + m_{PD} \right) \quad (43)$$

with constraints:

$$h(\mathbf{x}) = \mathbf{0} \quad (44)$$

$$g(\mathbf{x}) \leq \mathbf{0} \quad (45)$$

$$\mathbf{A} \cdot \mathbf{x} \leq \mathbf{b} \quad (46)$$

$$\mathbf{lb} \leq \mathbf{x} \leq \mathbf{ub} \quad (47)$$

with $\mathbf{x} = (D_o, D_i, \gamma, l_{axial}, n_{PG}, \rho)$ the design parameter vector and \mathbf{X} the design vector space. M_{motor} , m_{PG} and m_{PD} is the total (i.e., including end-windings) motor mass, gearbox mass and differential mass, respectively. The function $h(\mathbf{x})$ of Equation (44) contains the load cycle profile (Section 2.1) constraint which the design needs to be able

to follow. The function $g(\mathbf{x})$ of Equation (45) contains the maximum back-emf, current limit, ... constraints (Table 3). Equation (46) represents the physical geometrical constraints, e.g., the outer > inner diameter, ... Equation (47) represents the limits wherein the parameters can vary such as maximum dimension, maximum gearbox ratio, ... The upper and lower bound is given by \mathbf{ub} and \mathbf{lb} , respectively. Table 3 contains the specific values. Some of the constraints, i.e., Equations (44) and (45), are actually checked and applied in the “velocity distribution optimization” section of the procedure. As mentioned in Section 2.2.2, the differential introduces a mechanical degree-of-freedom. Therefore, the velocity distribution between the sun and ring branch needs to be calculated within the new design evaluation. This is done in the “velocity distribution optimization” section. The motor of this topology is electromagnetically designed in such a way that the two rotor-stator pairs can be modelled as two independent motors, an inrunner and an outrunner motor. The mechanical interconnection can be seen in Figure 3. The inertia of the motor, the mass of the motor and the no-load flux are velocity-independent and are calculated before the “velocity distribution optimization” section. The no-load flux is obtained from the response surface as explained in Section 2.5.4 given the cross-sectional parameters of the new design point. The internal optimizer used in the “velocity distribution optimization” section gives the angular velocity over the cycle for one of the branches by discretizing the cycle into N discretization points, see Table 12. The sun branch is chosen here. The velocity of the ring branch is obtained through the differential angular velocity constraint (Equation (8)) given the sun branch and the carrier branch angular velocity. At every discretization point, the angular velocity of the sun branch is chosen by the optimizer. Using numerical differentiation, the angular acceleration can be calculated such that the inertial torques are obtained. The energy loss over the cycle is obtained using numerical integration of the power losses during the cycle. The general mathematical form of the internal “velocity distribution optimization”:

$$\mathbf{x}_\omega^* = \min_{\mathbf{x}_\omega \in \mathbf{X}_\omega} (E_{l,mech} + E_{l,motor}) \quad (48)$$

with active constraints:

$$h_\omega(\mathbf{x}_\omega) = \mathbf{0} \quad (49)$$

$$g_\omega(\mathbf{x}_\omega) \leq \mathbf{0} \quad (50)$$

$$\mathbf{lb}_\omega \leq \mathbf{x}_\omega \leq \mathbf{ub}_\omega \quad (51)$$

\mathbf{x}_ω is the angular velocity vector and \mathbf{X}_ω is the angular velocity space. The function $h_\omega(\mathbf{x}_\omega)$ of Equation (49) contains the load cycle profile (Section 2.1) constraint which the design needs to be able to follow. The function $g_\omega(\mathbf{x}_\omega)$ of Equation (50) contains the maximum back-emf, current limit, ... constraints (Table 3). Equation (51) represents the limits wherein the velocity of the two branches can vary. This limit is obtained through the maximum allowable centrifugal force. The upper and lower bound is given by \mathbf{ub}_ω and \mathbf{lb}_ω , respectively. The internal optimization procedure goes as follows. First, it is checked if the voltage supplied from the source (V_{phase}) is high enough to overcome the maximum back-emf during the cycle. If the answer is no, the proposed velocity profile is rejected. Otherwise, the total torque (i.e., the load and inertial torque) is calculated. This part has interaction with the gearbox data. The smallest gearbox and differential to withstand the total torque is chosen. Once the torque is known, the necessary stator currents can be calculated. The currents are limited to the maximum RMS current density given in Table 3. If the RMS current density over the cycle is lower than this limit, the profile is accepted. Subsequently, the motor and drivetrain losses can be calculated. The value of the losses and the total mass of the topology is given back to the multi-objective optimizer and a new design point is chosen until the Pareto front converges. For the multi-objective optimization (i.e., the outer loop), the “gamultiobj” function of Matlab is used. This is a variant of the well-known and widely applied NSGA-II algorithm. The inner loop optimization uses the

“ga” function of Matlab. The same optimization procedure is used for topology T2.b. The optimization vector \mathbf{x}_ω now also contains the braking decisions which is either both brakes disengaged or one of the two brakes engaged while the other is disengaged. The braking decisions are given every L_b discretization points, see Table 12. The option of engaging both brakes is excluded since this option is not possible due to the kinematic requirements.

Table 12. Discretization parameters for the extended comparison.

Name	Symbol	Value	Unit
Number of discretization points	N	171	-
Number of discretization points per braking interval	L_b	9	-
Number of braking intervals	$N_b = N/L_b$	19	-

Once the Pareto-front of topology T2 and T2.b is known, the optimization of the other two topologies T1 and T4 can start. As mentioned at the start of this section, topology T1 and T4 are optimized with the constraint of a given active motor mass where the optimizer chooses the cross-sectional parameters (also the drivetrain parameters) and the motor is axially scaled to match the active motor mass. The optimization procedures for topology T1 and T4 seem similar to the procedure of topology T2 and T2.b. However, there are some important differences. For topology T1, there is no degree-of-freedom once the design point is chosen by the optimizer. Therefore, the load cycle and the design point completely define the performance of the design over the load cycle and no internal optimization is needed. The maximum back-emf and current constraint is again checked. The high-level mathematical representation of Equations (43)–(47) can be used for topology T1 with the following in mind. The design point, the active motor mass constraint, the voltage and current constraints completely define the torque-speed characteristic of the motor. Furthermore, as mentioned earlier, the smallest gearbox, i.e., the gearbox with the lowest mass which can withstand the torque transmitted over the cycle is chosen. Furthermore, with the absence of a differential, i.e., $m_{PD} = 0$, the multi-objective optimization can be reduced to a single-objective optimization with objective function the losses. The design vector is now $\mathbf{x} = (D_{s,o}, D_{s,i}, n_{PG})$ and $h(\mathbf{x})$ also contains the active motor mass constraint. The above explanation for topology T1 is also valid for topology T4 except there is an electromagnetic degree-of-freedom namely the electromagnetic torque distribution between the inner and outer stator. The design vector is now $\mathbf{x} = (D_{os,o}, D_{os,i}, D_{is,i}, n_{PG})$ and $h(\mathbf{x})$ again contains the active motor mass constraint. An internal optimization is required similar to topology T2 and T2.b but now for the torques. One of the two stators can be chosen for this. Once one of the two is known, the other torque can be calculated using the electromagnetic torque balance Equation (34) and the load torque on the rotor as input. The general mathematical form of the internal optimization:

$$\mathbf{x}_T^* = \min_{\mathbf{x}_T \in \mathbf{X}_T} (E_{l,mech} + E_{l,motor}) \quad (52)$$

with active constraints:

$$h_T(\mathbf{x}_T) = \mathbf{0} \quad (53)$$

$$g_T(\mathbf{x}_T) \leq \mathbf{0} \quad (54)$$

$$\mathbf{l}\mathbf{b}_T \leq \mathbf{x}_T \leq \mathbf{u}\mathbf{b}_T \quad (55)$$

\mathbf{x}_T is the outer stator torque vector and \mathbf{X}_T is the outer stator torque space. The function $h_T(\mathbf{x}_T)$ of Equation (53) contains the load cycle profile (Section 2.1) constraint which the design needs to be able to follow. The function $g_T(\mathbf{x}_T)$ of Equation (54) contains the maximum back-emf limit, the current limit, ... constraints (Table 3). Equation (55) represents the limits wherein the torques of the two branches can vary. The upper and lower bound is given by $\mathbf{u}\mathbf{b}_T$ and $\mathbf{l}\mathbf{b}_T$, respectively.

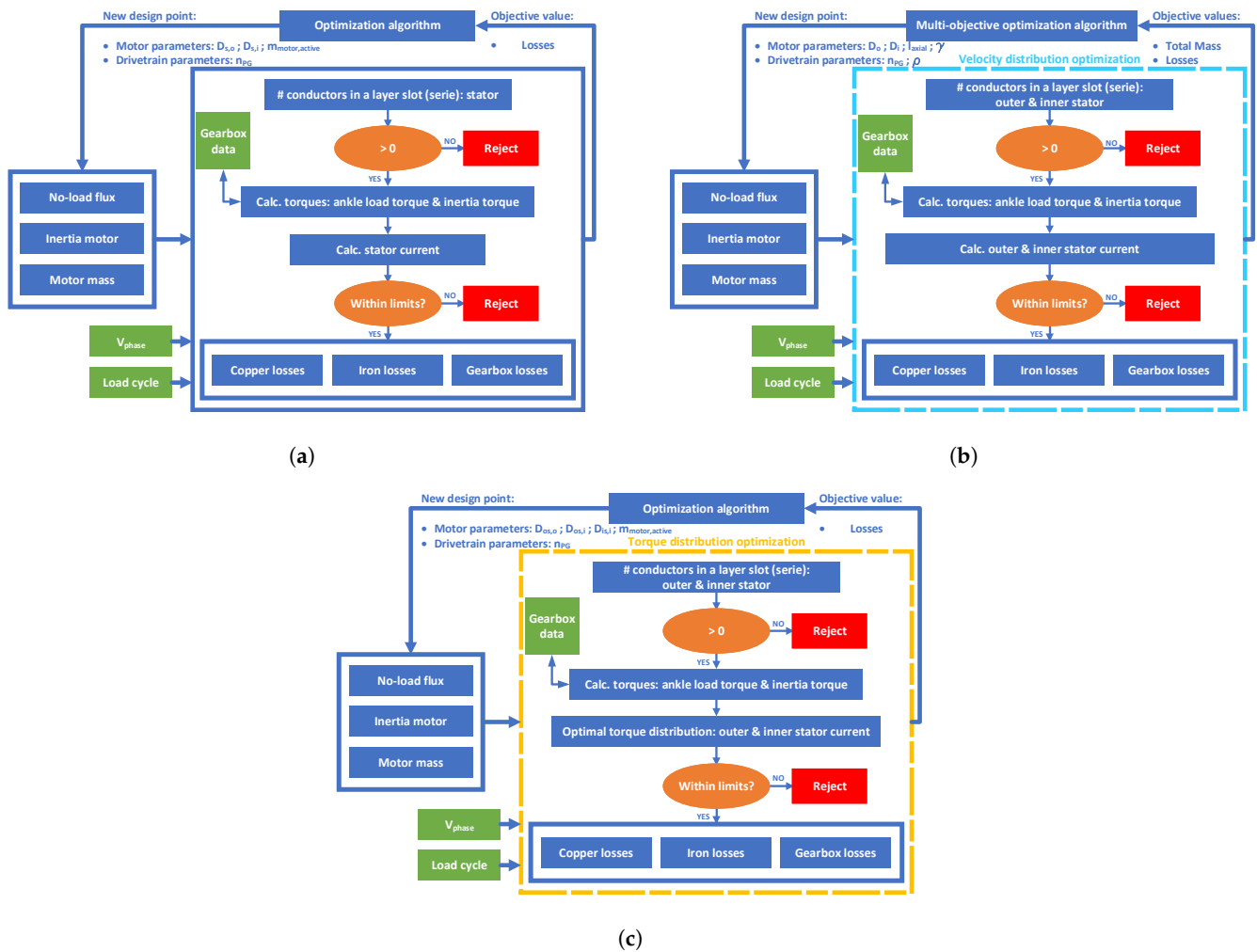


Figure 11. Optimization flowchart (a) Topology T1 (b) Topology T2 and T2.b (c) Topology T4.

3. Results

3.1. Basic Comparison

The results of the basic comparison are shown in Tables 13–17 for topology T1, T2, T2.b, T3 and T4, respectively. The mark “x” means that no result which satisfies the constraints is found. The cell color gives a visual representation of the performance. The performance decreases, i.e., a higher cost function value, with increasing color intensity. The scaling is the same for all the above mentioned tables. For topology T1 (Table 13), the cost decreases with decreasing reflected inertia to the rotor (J) and thus decreasing inertial torque. For the topology T2, a smaller inertia reflected to the outer rotor (J_{or}) reduces the cost over one cycle. The inertia reflected to the inner rotor (J_{ir}) has a less pronounced influence on the cost. However, the change of J_{ir} from $1 \times 10^{-3} \text{ kg}\cdot\text{m}^2$ to $1 \times 10^{-5} \text{ kg}\cdot\text{m}^2$ with a J_{or} of $1 \times 10^{-3} \text{ kg}\cdot\text{m}^2$ reduces the cost by $\pm 40\%$. The same reducing effect can be seen for a J_{or} of $1 \times 10^{-4} \text{ kg}\cdot\text{m}^2$ although less significant. The effect of J_{or} and J_{ir} on the cost of topology T3 is more pronounced. A lower J_{or} results in a lower cost. The opposite is true for J_{ir} , a lower inertia increases the cost. Topology T4 can give insight in this phenomena as it can be seen as a special case of topology T3. Topology T4 can be seen as topology T3 with a blocked inner rotor or an inner rotor with infinite inertia such that a finite net torque, i.e., the integral of the torque over the cycle, results in zero acceleration. Thus, a finite net torque delivery of the inner rotor would result in no velocity variation over the cycle. The topologies T1 and T4 are similar that there is only one rotor. The results for topology T4 are shown in Table 17. The objective function decreases with decreasing reflected inertia to the rotor (J). The objective function value of topology T4 compared to topology T1 (Table 13)

is about half. This can be explained by the following observation. The load torque will be evenly, same weight in the objective function, distributed between the inner and outer stator. For topology T1 on the other hand, this is not possible. Using the objective functions defined in Table 1:

$$f_{T_1} = \int_0^{T_{\text{cycle}}} T_l(t)^2 dt \quad (56)$$

$$f_{T_4} = \int_0^{T_{\text{cycle}}} \left[(T_l(t)/2)^2 + (T_l(t)/2)^2 \right] dt = \frac{1}{2} \int_0^{T_{\text{cycle}}} T_l(t)^2 dt \quad (57)$$

$$\rightarrow \frac{f_{T_1}}{f_{T_4}} = 2 \quad (58)$$

where $T_l(t)$ stands for the total load torque, i.e., the load torque and inertial torque combined. A given inertia results in the same inertial torque for both topologies since the kinematic profile for the single rotor of both topologies is the same. It can thus be concluded that the extra degree-of-freedom due to the extra stator reduces the cost over the cycle significantly. Finally, topology T2.b shows the best energetic performance and increases the inertia cases for which a solution can be found. In order to understand why, the braking vectors containing the braking states on each braking interval is given as well, see Table 15. The results obtained for a J_{ir} of 1×10^{-2} and $1 \times 10^{-3} \text{ kg}\cdot\text{m}^2$ are similar to those of topology T2. A slight energetic improvement is obtained. The inner rotor branch is blocked on all these cases except for ($J_{ir} = 1 \times 10^{-3} \text{ kg}\cdot\text{m}^2$, $J_{or} = 1 \times 10^{-3} \text{ kg}\cdot\text{m}^2$). Both brakes are disengaged during the first braking interval for this specific case. The differential acts as a gearbox on all the other intervals. The load torque seen by the motor is slightly reduced to the outer rotor branch with a gear ratio of $\frac{1+\rho}{\rho}$. This explains the slight decrease in the objective value. The addition of the brakes has a significant impact on the cases with a J_{ir} of 1×10^{-4} and $1 \times 10^{-5} \text{ kg}\cdot\text{m}^2$. For 6 out of the 8 cases, the outer rotor branch is blocked during the whole cycle, i.e., only '2' in the braking vector. For a high J_{or} and a low J_{ir} , it is energetically more efficient to only let the inner rotor branch rotate. The differential again acts as a gearbox. The load torque seen by the motor is reduced to the inner rotor branch with a gear ratio of $1 + \rho$. Furthermore, since the inertia of this branch is so low, the inertial torque is limited compared to the load torque. The cases ($J_{ir} = 1 \times 10^{-4} \text{ kg}\cdot\text{m}^2$, $J_{or} = 1 \times 10^{-4} \text{ kg}\cdot\text{m}^2$) and ($J_{ir} = 1 \times 10^{-4} \text{ kg}\cdot\text{m}^2$, $J_{or} = 1 \times 10^{-5} \text{ kg}\cdot\text{m}^2$) are the only cases with a diverse braking pattern over the cycle. They are similar and the only difference is located at the seventh braking interval. During the first braking interval, both rotors are allowed to rotate. From interval 2 to 4, only the inner rotor branch is allowed to rotate. During the fifth interval, both branches rotate again. During this interval, the torque and angular velocity of the ankle reaches the maximum absolute value. From the sixth interval onwards, the ankle torque is close to zero. The outer rotor branch contributes more to the output velocity (Equation (8)). Thus, for a low J_{or} , it is energetically interesting to only rotate the outer rotor branch due to the low load torque and the low inertial torque.

Table 13. Results of topology T1: objective function value for different reflected rotor inertia J , "x": no solution which satisfies the constraints is found.

J [$\text{kg}\cdot\text{m}^2$]	1×10^{-2}	1×10^{-3}	1×10^{-4}	1×10^{-5}
$f_{opt}(J)$	x	4.0567	2.1181	2.0231

Table 14. Results of topology T2: objective function value for different reflected inner J_{ir} and outer J_{or} rotor inertia, “x”: no solution which satisfies the constraints is found.

J_{or} [kg·m ²]	J_{ir} [kg·m ²]	1×10^{-2}	1×10^{-3}	1×10^{-4}	1×10^{-5}
1×10^{-2}		x	x	x	x
1×10^{-3}		3.9469	3.9409	x	2.3747
1×10^{-4}		1.7478	1.75	1.7604	1.6972
1×10^{-5}		1.65	1.6502	1.6523	1.6607

Table 15. Results of topology T2.b: objective function value and braking vector for different reflected inner J_{ir} and outer J_{or} rotor inertia (0: both brakes disengaged, 1: inner rotor branch brake engaged and outer rotor branch brake disengaged, 2: outer rotor branch brake engaged and inner rotor branch brake disengaged), “x”: no solution which satisfies the constraints is found.

J_{or} [kg·m ²]	J_{ir} [kg·m ²]	1×10^{-2}	1×10^{-3}	1×10^{-4}	1×10^{-5}
1×10^{-2}		x	x	1.221 [2 2 2 2 2 2 2 2]	0.0406 [2 2 2 2 2 2 2 2]
1×10^{-3}		3.9401 [1 1 1 1 1 1 1 1]	3.9381 [0 1 1 1 1 1 1 1]	1.221 [2 2 2 2 2 2 2 2]	0.0406 [2 2 2 2 2 2 2 2]
1×10^{-4}		1.7388 [1 1 1 1 1 1 1 1]	1.7388 [1 1 1 1 1 1 1 1]	0.6508 [0 2 2 2 0 1 0 1]	0.0406 [2 2 2 2 2 2 2 2]
1×10^{-5}		1.6406 [1 1 1 1 1 1 1 1]	1.646 [1 1 1 1 1 1 1 1]	0.5848 [0 2 2 2 0 1 1 1]	0.0406 [2 2 2 2 2 2 2 2]

Table 16. Results of topology T3: objective function value for different reflected inner J_{ir} and outer J_{or} rotor inertia, “x”: no solution which satisfies the constraints is found.

J_{or} [kg·m ²]	J_{ir} [kg·m ²]	1×10^{-2}	1×10^{-3}	1×10^{-4}	1×10^{-5}
1×10^{-2}		x	x	x	x
1×10^{-3}		2.427	2.427	2.9907	4.004
1×10^{-4}		1.4523	1.4523	1.6957	2.0875
1×10^{-5}		1.4047	1.4048	1.6278	1.9944

Table 17. Results of topology T4: objective function value for different reflected rotor inertia J , “x”: no solution which satisfies the constraints is found.

J [kg·m ²]	1×10^{-2}	1×10^{-3}	1×10^{-4}	1×10^{-5}
$f_{opt}(J)$	x	2.0338	1.0591	1.0115

3.2. Extended Comparison

3.2.1. Mass-Energy Loss Trade-Off Characteristics

From Figure 12, the trade-off between mass and energy loss is immediately visible. It is also clear that the level of trade-off is different from topology to topology.

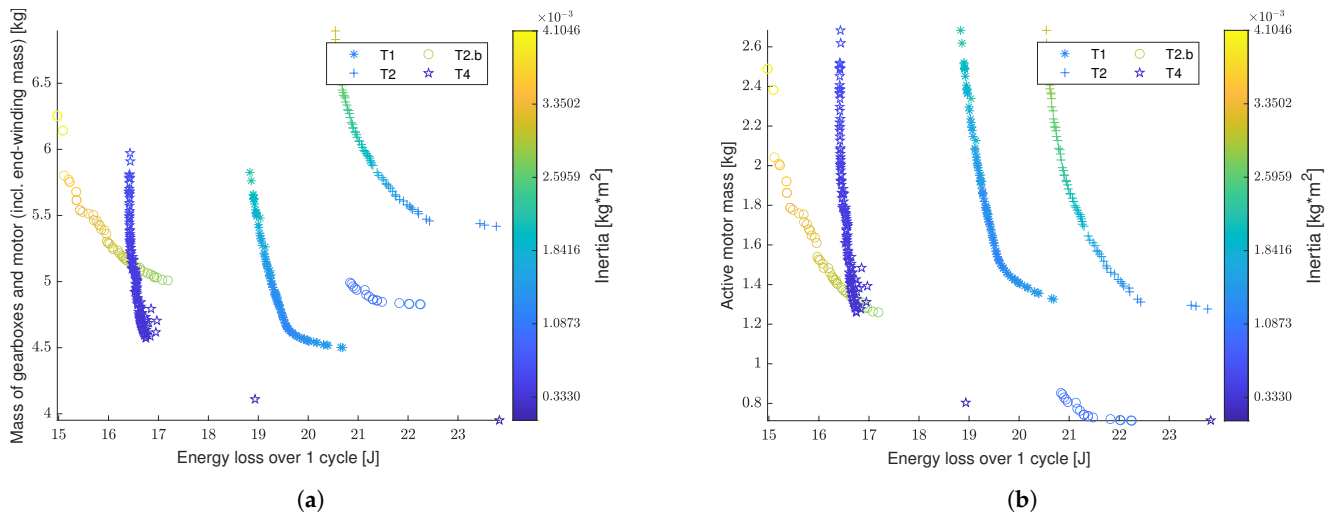


Figure 12. Results of the optimization for the different topologies: (a) Considering the total drive-train mass, i.e., total motor mass (active and endwindings) and the mass of all the gearboxes and differentials if present in the topology. (b) Only considering the active mass of the motor.

All the topologies show a clear inverse relation between mass and energy loss. For topology T4, this is less pronounced. However, this relation is present when looking at the points above 1.2 kg active motor mass and below. The found solutions above 1.2 kg active motor mass are located in the quasi-vertical region of the trade-off. This is similar to the behaviour seen for the topologies T1, T2 and T2.b. The found solutions below 1.2 kg active motor mass belong to the quasi-horizontal region of the trade-off. This is also similar to the behaviour of the other topologies. From Figure 12a, it can be concluded that topology T4 is the best solution if both energy loss and total topology mass are taken into account. If only energy efficiency is important, the topology T2.b gives the best results. The objective values of the solutions of topology T2.b show a clear jump in regions on the mass-energy loss plane. As was mentioned earlier, the brakes introduce a discontinuity in the system. This manifests itself by the jump in the objective space. As can be noticed in Figure 12b, the added brakes in topology T2.b allow to find a solution below the active mass level of 1.2 kg. No solutions of topology T1 and T2 are found below 1.2 kg active motor mass. For topology T4, a small amount of solutions are found with a relatively high loss compared to the solutions found above the 1.2 kg active mass level. The topologies T4 and T1 contain one less loss component, i.e., no differential, compared to the topologies T2 and T2.b. This explains the total mass shift of topology T2 and T2.b compared to the topologies T1 and T4 although the active motor mass is the same. The absence of the differential results in less mechanical losses due to no additional meshing losses in the differential. Another reason for the higher energy loss of topology T2 is the additional inertia introduced into the system. As shown in Figure 1, the ankle gait cycle is highly dynamic with fast ascends and descends of the velocity profile. The inertia is therefore an important parameter that influences the performance of a topology. The color of the solution points of all topologies in Figure 12 change according to the inertia of the motor rotor. For topology T2 and T2.b, this is the inertia of the rotor connected to the ring and the ring gear inertia. The inertia of the rotor connected to the sun and the sun gear inertia is of the order 1×10^{-4} to $1 \times 10^{-5} \text{ kg}\cdot\text{m}^2$ with a similar variation as function of the active motor mass as for the ring branch inertia. As can be expected, the inertia increases with increasing active motor mass. According to Section 3.1, it would be expected that the energy loss of all topologies would increase with

increasing inertia. However, the used cost functions in Section 3.1 are very basic and do not account for the motor geometrical influence on the energy loss. The mechanical losses introduced by the gearbox and differential if present were not included in Section 3.1.

3.2.2. Loss Decomposition

Figure 13 shows the energy loss distribution over 1 cycle as function of the active motor mass for all the topologies. The losses are stacked in Figure 13.

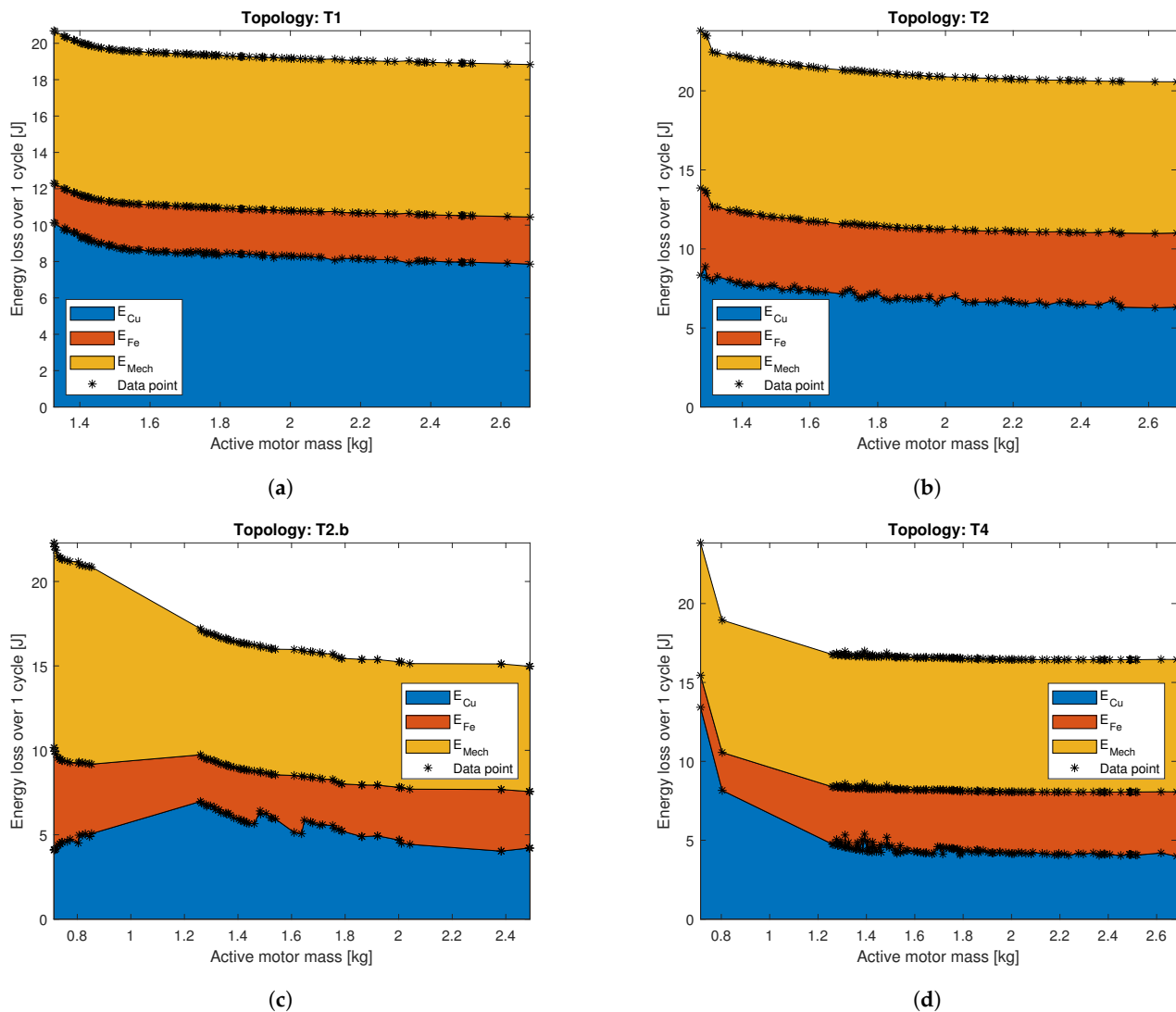


Figure 13. Energy loss distribution as function of the active motor mass for (a) Topology T1 (b) Topology T2 (c) Topology T2.b (d) Topology T4.

First of all, notice the difference in the lower limit of the active motor mass (x-axis) for the different topologies. For topology T1 and T2 (Figure 13a,b), the iron and mechanical loss is relatively constant over the whole mass range. The copper loss slowly decreases with increasing motor mass. For topology T4, the iron loss increases significantly from the lower limit of the active motor mass to approximately 1.2 kg. Afterwards, the iron loss is relatively constant. The copper loss also changes significantly within this lower mass area. It sharply decreases with increasing mass and it stabilizes again after the 1.2 kg mark. The mechanical energy loss remains quasi constant over the mass range. Thus, after the 1.2 kg mark, the loss behaviour of topology T4 is similar to topology T1 and T2. Topology T2.b has a different shape at the lower mass region. The copper loss increases at first. After the 1.2 kg mark, it slowly decreases although with a zigzag pattern. The energy

loss curve is less smooth compared to the other topologies. This is caused by the brakes and the consequently discontinuous behaviour in the system. The iron loss has the inverse behaviour, i.e., it first decreases to slowly increase again. The mechanical energy loss is high at low active mass. It stabilizes at 1.2 kg. The mechanical energy loss for topology T2.b past the 1.2 kg mark is the lowest of all topologies. From Figure 13, the relative loss contribution can be ranked in decreasing order: mechanical loss, copper loss and iron loss.

3.2.3. Braking Behaviour

In order to understand the workings of the added brakes in topology T2.b, the cumulative braking state over the ankle cycle is given in Figure 14.

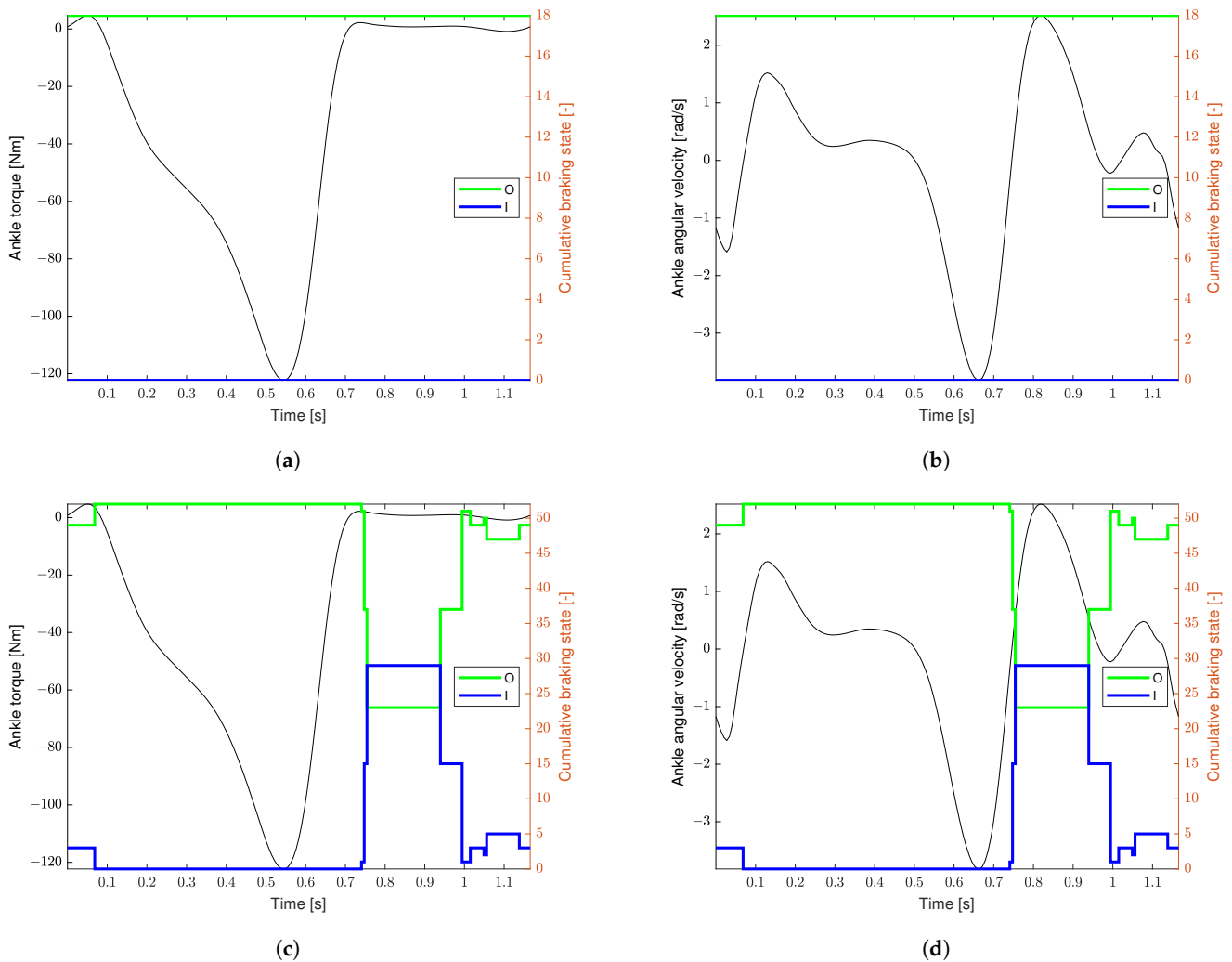


Figure 14. Cumulative braking states of topology T2.b over the ankle cycle. (a) Ankle torque cycle: design points above 19 J total energy loss (18 points) (b) Ankle angular velocity cycle: design points above 19 J total energy loss (18 points) (c) Ankle torque cycle: design points below 19 J total energy loss (52 points) (d) Ankle angular velocity cycle: design points below 19 J total energy loss (52 points).

The cumulative braking state on a braking interval is defined as:

$$CBS_{i,l} = \sum_{k=1}^N (\delta_b)_{i,k} \quad (59)$$

where i stands for the outer rotor branch 'O' or inner rotor branch 'I'. 'I' is the braking interval index, i.e., $l = 1 \dots N_b$. Furthermore, 'N' is the number of considered design points.

The Pareto front of topology T2.b in Figure 12 has two distinguished regions. A region of points below 19 J energy loss and a region above 19 J energy loss. Therefore, the analysis of the braking behaviour is split into these two regions. Figure 14a,b show the braking behaviour for the points in the region above 19 J energy loss. All these points have a blocked outer rotor branch and a free inner rotor branch for the complete ankle cycle. The outer rotor is therefore unused and unnecessary. The differential acts as a simple gearbox in this case with a gear ratio of $(\rho + 1)$. The Pareto front points located below 19 J energy loss show more variation in the braking behaviour in certain regions of the cycle. This can be seen in Figure 14c,d. The biggest difference is seen in the 0.75 to 1 s region of the cycle which is part of the swing phase of the ankle cycle, see Section 2.1. Notice that either the inner rotor or the outer rotor is unlocked while the other rotor is locked. This can be verified by taking the sum of the $CBS_{O,l}$ and $CBS_{I,l}$ on each braking interval l during this phase. This sum equals the number of design points N , 52 in this case. Since locking of both rotors simultaneously on the same braking interval is impossible, locking of one rotor while unlocking of the other rotor is the only possible solution. From 0.75 to 1 s, the outer rotor branch is locked less than the inner rotor branch on average. The demanded load torque by the ankle is close to zero during this interval. Recall from Equation (7) that the outer rotor branch receives $C_{PD} \cdot \rho$ more load torque compared to the inner rotor branch. On the other hand, the outer rotor branch contributes more to the output velocity of the differential, see Equation (8). A larger motor results in more inertia of the rotors and thus also the inner rotor. Therefore, the inertial torque for the inner rotor can become significant compared to the load torque in the swing phase. Thus, it becomes interesting for the outer rotor branch to take over during periods of low load torque. The most efficient rotor which can fulfill the load profile is chosen. This mainly depends on the reflected inertia to the rotor, the load profile reflected to the rotor and the torque per unit power loss of each rotor. For the Pareto points above 19 J energy loss, the inner rotor branch inertia is very low and as a result also the inertial torque. The unlocking of the outer rotor branch in these cases is not needed from an energetic point of view. This behaviour is similar to the one seen in Section 3.1.

3.2.4. Qualitative Assessment: Radar Plot

Figure 15 shows a radar plot to qualitatively assess the topologies. The performance indicators are energetic performance, total mass of the topology and complexity. The complexity increases with increasing amount of components and increasing degrees-of-freedom, mechanically and electrically. Topology T1 scores the best on the complexity indicator. Topology T2.b has the best energetic performance. Furthermore, topology T4 has the lowest total mass, so a high score on the total mass indicator. When looking at the overall performance of the topologies (i.e., area spanned by the triangles), the topologies can be ordered as, ranked from high overall performance to low: T4 (dual-stator motor), T1 (outrunner PMSM), T2.b (dual-rotor motor with brakes) and T2 (dual rotor motor).

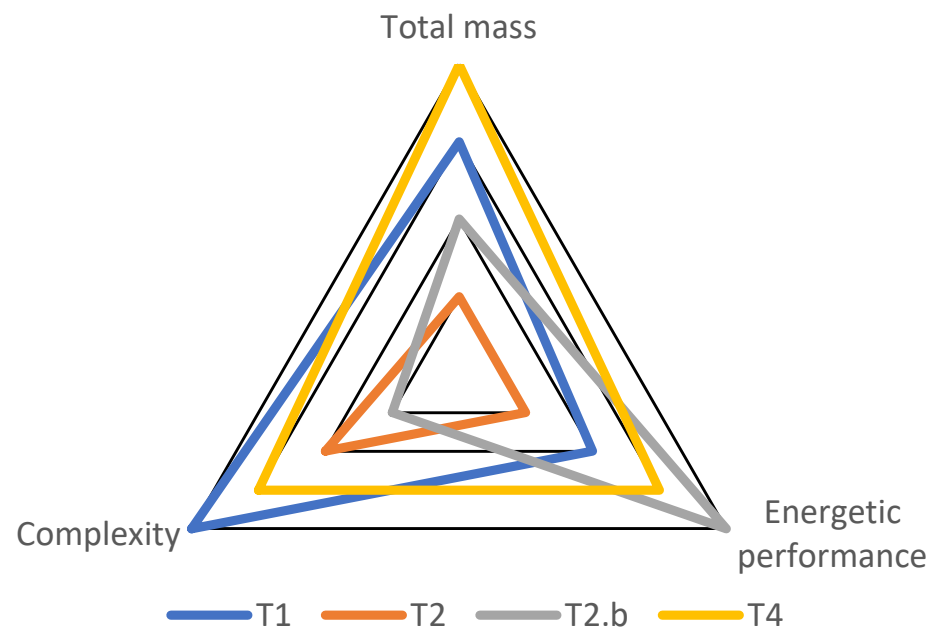


Figure 15. Qualitative comparison of the different topologies, increasing performance on the specific performance indicator from inside to outside.

4. Conclusions

In this work, multiple topologies were compared using the gait cycle of a human ankle as a case study. This type of cycle is commonly found in prosthesis actuation. It is a challenging cycle for a single direct-drive motor. First, a basic comparison was done where the focus was purely on the kinematic and dynamic performance of the topologies with simple cost functions. Topology T2.b (dual-rotor motor with brakes) showed the best performance followed by topology T4 (dual-stator motor), T3 (dual-rotor motor with flywheel), T2 (dual-rotor motor) and T1 (outrunner PMSM) in order of decreasing performance. Afterwards, an extended comparison was done using more in-depth cost functions including motor losses (copper and iron losses) and drivetrain losses (gearbox and differential losses if present). The mass of the topology was also taken into account during this comparison. Topology T1 has the least amount of complexity, i.e., best complexity score, while still performing well in terms of total mass and energetic performance. Topology T4 shows the best overall performance when considering the whole picture of energetic performance, total mass and complexity (Figure 15). Topology T2.b has the best energetic performance of all the considered topologies but at the cost of an increased total mass and complexity. The braking system was modeled under certain assumptions (see Section 2.2.4) which resulted in an idealized brake model. Depending on the practical implementation of the braking system, one or more of these assumptions will be violated. This will affect the performance of the topology. Topology T2 is the worst overall performing topology. This result is different compared to the basic comparison. Depending on the weights given to the three different performance indicators (i.e., complexity, energetic performance and total mass) by the designer, one topology is preferred over the other (Figure 15). Thus, topology T2.b and topology T4 have the potential to reduce the energy consumption compared to traditional solutions with a limited addition of mass. The addition of brakes (Topology T2.b) improved the mass and energetic performance significantly compared to the original topology (Topology T2). This work also showed that a comparison between topologies requires in-depth models of all the sub-components present in a topology. In future studies, the following ideas could be investigated: (1) the influence of different cost functions, (2) the influence of the Coulomb and viscous friction terms and (3) the influence of an adaptive discretization mesh.

Author Contributions: Conceptualization, Y.J.; methodology, Y.J.; software, Y.J.; validation, Y.J.; formal analysis, Y.J.; investigation, Y.J.; resources, Y.J.; data curation, Y.J.; writing—original draft preparation, Y.J.; writing—review and editing, P.S., H.V. and T.V.; visualization, Y.J.; supervision, P.S., H.V. and T.V. All authors have read and agreed to the published version of the manuscript.

Funding: This work was partially supported by the Research Foundation-Flanders (FWO), grant no. 1505820N.

Data Availability Statement: The study did not report any data.

Conflicts of Interest: The authors declare no conflict of interest.

References

1. Verstraten, T.; Geeroms, J.; Mathijssen, G.; Convens, B.; Vanderborght, B.; Lefeber, D. Optimizing the power and energy consumption of powered prosthetic ankles with series and parallel elasticity. *Mech. Mach. Theory* **2017**, *116*, 419–432. [\[CrossRef\]](#)
2. Babič, J.; Laffranchi, M.; Tessari, F.; Verstraten, T.; Novak, D.; Šarabon, N.; Ugurlu, B.; Peternel, L.; Torricelli, D.; Veneman, J.F. Challenges and solutions for application and wider adoption of wearable robots. *Wearable Technol.* **2021**, *2*, e14. [\[CrossRef\]](#)
3. Seok, S.; Wang, A.; Chuah, M. Y.; Hyun, D. J.; Lee, J.; Otten, D. M.; Lang, J. H.; Kim, S. Design Principles for Energy-Efficient Legged Locomotion and Implementation on the MIT Cheetah Robot. *IEEE/ASME Trans. Mechatron.* **2015**, *20*, 1117–1129. [\[CrossRef\]](#)
4. Zhu, J.; Jiao, C.; Dominguez, I.; Yu, S.; Su, H. Design and Backdrivability Modeling of a Portable High Torque Robotic Knee Prosthesis with Intrinsic Compliance for Agile Activities. *IEEE/ASME Trans. Mechatron.* **2022**, *4*, 1837–1845. [\[CrossRef\]](#)
5. Grandesso, G.; Bravo-Palacios, G.; Wensing, P.M.; Fontana, M.; Prete, A.D. Exploring the Limits of a Redundant Actuation System through Co-Design. *IEEE Access* **2021**, *9*, 56802–56811. [\[CrossRef\]](#)
6. Sánchez Barrera, A.; Ortega Blanco, A.; Rayón Martínez, E.; Becerra Gómez, F.A.; Pliego Abúndez, A.; Amezcua Campos, R.; Valdivia Guzmán, C.H. State of the Art Review of Active and Passive Knee Orthoses. *Machines* **2022**, *10*, 865. [\[CrossRef\]](#)
7. Pan, C.T.; Lee, M.C.; Huang, J.S.; Chang, C.C.; Hoe, Z.Y.; Li, K.M. Active Assistive Design and Multiaxis Self-Tuning Control of a Novel Lower Limb Rehabilitation Exoskeleton. *Machines* **2022**, *10*, 318. [\[CrossRef\]](#)
8. Girard, A.; Asada, H.H. Leveraging Natural Load Dynamics with Variable Gear-Ratio Actuators. *IEEE Robot. Autom. Lett.* **2017**, *2*, 741–748. [\[CrossRef\]](#)
9. Verstraten, T.; Furnémont, R.; López-García, P.; Crispel, S.; Vanderborght, B.; Lefeber, D. A series elastic dual-motor actuator concept for wearable robotics. *Biosyst. Biorobotics* **2019**, *22*, 165–169. [\[CrossRef\]](#)
10. Verstraten, T.; Furnémont, R.; López-García, P.; Rodríguez-Cianca, D.; Vanderborght, B.; Lefeber, D. Kinematically redundant actuators, a solution for conflicting torque–speed requirements. *Int. J. Robot. Res.* **2019**, *38*, 612–629. [\[CrossRef\]](#)
11. Mantriota, G.; Reina, G. Dual-motor planetary transmission to improve efficiency in electric vehicles†. *Machines* **2021**, *9*, 58. [\[CrossRef\]](#)
12. De Carlo, M.; Mantriota, G. Electric vehicles with two motors combined via planetary gear train. *Mech. Mach. Theory* **2020**, *148*, 103789. [\[CrossRef\]](#)
13. Chen, H.; Liu, X.; Zhao, J.; Demerdash, N.A. Magnetic-Coupling Characteristics Investigation of a Dual-Rotor Fault-Tolerant PMSM. *IEEE Trans. Energy Convers.* **2018**, *33*, 362–372. [\[CrossRef\]](#)
14. Allahyari, A.; Torkaman, H. A Novel High-Performance Consequent Pole Dual Rotor Permanent Magnet Vernier Machine. *IEEE Trans. Energy Convers.* **2020**, *35*, 1238–1246. [\[CrossRef\]](#)
15. Druant, J. Modeling and Control of an Electrical Variable Transmission with Hybrid Excitation. Ph.D. Thesis, Faculty of Engineering and Architecture, Ghent University, Ghent, Belgium, 2018.
16. Li, C.; Guo, X.; Fu, J.; Fu, W.; Liu, Y.; Chen, H.; Wang, R.; Li, Z. Design and Analysis of a Novel Double-Stator Double-Rotor Motor Drive System for In-Wheel Direct Drive of Electric Vehicles. *Machines* **2022**, *10*, 27. [\[CrossRef\]](#)
17. Furnémont, R.; Mathijssen, G.; Verstraten, T.; Jimenez-Fabian, R.; Lefeber, D.; Vanderborght, B. Novel control strategy for the +SPEA: A redundant actuator with reconfigurable parallel elements. *Mechatronics* **2018**, *53*, 28–38. [\[CrossRef\]](#)
18. Verstraten, T.; Furnémont, R.; López-García, P.; Rodríguez-Cianca, D.; Cao, H.L.; Vanderborght, B.; Lefeber, D. Modeling and design of an energy-efficient dual-motor actuation unit with a planetary differential and holding brakes. *Mechatronics* **2018**, *49*, 134–148. [\[CrossRef\]](#)
19. Wang, Y.; Fu, W.N.; Niu, S. A Novel Structure of Dual-Stator Hybrid Excitation Synchronous Motor. *IEEE Trans. Appl. Supercond.* **2016**, *26*, 0605805. [\[CrossRef\]](#)
20. Zhang, J.; Zhang, B.; Feng, G.; Gan, B. Design and analysis of a low-speed and high-torque dual-stator permanent magnet motor with inner enhanced torque. *IEEE Access* **2020**, *8*, 182984–182995. [\[CrossRef\]](#)
21. Winter, D.A. *Biomechanics and Motor Control of Human Movement*; Wiley: Hoboken, NJ, USA, 2009; pp. 1–370. [\[CrossRef\]](#)
22. Verstraten, T. New Actuation Paradigms with High Efficiency for Variable Load at Varying Speed. Ph.D. Thesis, Vrije Universiteit Brussel, Belgium, Brussel, 2018.
23. Verstraten, T.; Mathijssen, G.; Furnémont, R.; Vanderborght, B.; Lefeber, D. Modeling and design of geared DC motors for energy efficiency: Comparison between theory and experiments. *Mechatronics* **2015**, *30*, 198–213. [\[CrossRef\]](#)

24. Park, R.H. Two-Reaction Theory of Synchronous Machines: Generalized Method of Analysis-Part I. *Trans. Am. Inst. Electr. Eng.* **1929**, *48*, 716–727. [[CrossRef](#)]
25. Duesterhoeft, W.C.; Schulz, M.W.; Clarke, E. Determination of Instantaneous Currents and Voltages by Means of Alpha, Beta, and Zero Components. *Trans. Am. Inst. Electr. Eng.* **1951**, *70*, 1248–1255. [[CrossRef](#)]
26. Carney, M.E.; Shu, T.; Stolyarov, R.; Duval, J.F.; Herr, H.M. Design and Preliminary Results of a Reaction Force Series Elastic Actuator for Bionic Knee and Ankle Prostheses. *IEEE Trans. Med Robot. Bionics* **2021**, *3*, 542–553. [[CrossRef](#)]
27. Azocar, A.F.; Mooney, L.M.; Duval, J.F.; Simon, A.M.; Hargrove, L.J.; Rouse, E.J. Design and clinical implementation of an open-source bionic leg. *Nat. Biomed. Eng.* **2020**, *4*, 941–953. [[CrossRef](#)]
28. Pyrhönen, J.; Jokinen, T.; Hrabovcová, V. *Design of Rotating Electrical Machines*; John Wiley & Sons: Hoboken, NJ, USA, 2008; pp. 1–512. [[CrossRef](#)]
29. Martínez, D. Design of a Permanent-Magnet Synchronous Machine with Non-Overlapping Concentrated Windings Design of a Permanent-Magnet Synchronous Machine with Non-Overlapping Concentrated Windings for the Shell Eco Marathon Urban Prototype. Master's Thesis, Royal Institute of Technology, Stockholm, Sweden, 2012.
30. Barré, O.; Napame, B. Concentrated windings in compact permanent magnet synchronous generators: Managing efficiency. *Machines* **2016**, *4*, 2. [[CrossRef](#)]
31. Choe, Y.Y.; Oh, S.Y.; Ham, S.H.; Jang, I.S.; Cho, S.Y.; Lee, J.; Ko, K.C. Comparison of concentrated and distributed winding in an IPMSM for vehicle traction. *Energy Procedia* **2012**, *14*, 1368–1373. [[CrossRef](#)]
32. Xu, Y.; Huang, X.; Chen, Z.; Zhang, J. Comparisons of Concentrated Fractional Winding and Distributed Winding of Permanent Magnet Synchronous Motors for Biped Robot. In Proceedings of the 2019 22nd International Conference on Electrical Machines and Systems, ICEMS 2019, Harbin, China, 11–14 August 2019; pp. 1–4. [[CrossRef](#)]
33. Saerens, E.; Crispel, S.; García, P.L.; Verstraten, T.; Ducastel, V.; Vanderborght, B.; Lefeber, D. Scaling laws for robotic transmissions. *Mech. Mach. Theory* **2019**, *140*, 601–621. [[CrossRef](#)]

Disclaimer/Publisher's Note: The statements, opinions and data contained in all publications are solely those of the individual author(s) and contributor(s) and not of MDPI and/or the editor(s). MDPI and/or the editor(s) disclaim responsibility for any injury to people or property resulting from any ideas, methods, instructions or products referred to in the content.